AUTOMATED RECONSTRUCTION OF NEUROVASCULAR NETWORKS IN KNIFE-EDGE SCANNING MICROSCOPE MOUSE AND RAT BRAIN NISSL STAINED DATA SETS

A Thesis

by

WOO KYUNG AN

Submitted to the Office of Graduate and Professional Studies of
Texas A&M University
in partial fulfillment of the requirements for the degree of

MASTER OF SCIENCE

Chair of Committee,	Yoonsuck Choe
Committee Members,	James Caverlee
	Peng Li
Head of Department,	Dilma Da Silva

August 2016

Major Subject: Computer Science

ABSTRACT

The Knife-Edge Scanning Microscope (KESM) developed at the Brain Network Laboratory at Texas A&M University can image a whole small animal brain at sub-micrometer resolution. Nissl data from the KESM enable us to look into vasculatures and cell bodies at the same time. Hence, analyzing the images from KESM mouse and rat Nissl data can help understand interactions between cerebral blood flow and its surrounding tissue. However, analysis is difficult since the image data contain complex cellular features as well as imaging artifacts, which make it hard to extract the geometry of the vasculature and the cells. In this project, we propose a novel approach to reconstructing the neurovascular networks from whole-brain mouse and partial rat Nissl data sets. The proposed method consists of (1) pre-processing, (2) thresholding, and (3) post-processing. Initially, we enhanced the raw image data in the pre-processing step. Next, we applied a dynamic global thresholding to extract vessels in the thresholding step. Subsequently, in the post-processing step, we computed local properties of the connected components to remove various sources of noise, and applied artificial neural networks to extract vasculatures. Concurrently, the proposed method connected small and large discontinuities in the vascular traces. To validate the performance of the proposed method, we compared reconstruction results of the proposed method with an alternative method (Lim's method). The comparison shows that the proposed method significantly outperforms (nine times faster, and more robust to noise) Lim's method. As a consequence, the proposed method provides a framework that can be applied to other data sets, even when the images contain a large portion of low-contrast images across the image stacks. We expect that the proposed method will contribute to studies investigating the

correlation between the soma of the cells and microvascular networks.

DEDICATION

To my parents, Sandong An and Namsun Moon,

My beloved wife, Heeyeon Chang,

My only brother, Taekyung An,

My future daughter, Suri An,

And my departed friend, Woosung Choi

ACKNOWLEDGEMENTS

I have been fortunate to have my advisor, Professor Yoonsuck Choe, who allowed this project to be my own research, and guided me in the right direction whenever he thought I needed it. Without his guidance and persistent help with this MS thesis project, I would not have been able to finish the project. I appreciate my parents who supported me and my wife emotionally and financially. I would like to thank my committee members, Professor James Caverlee and Professor Peng Li, who gave me valuable comments on my research. I would also like to thank a senior colleague, Jaewook Yoo, for his endless support. I also thank Junseok Lee and Michael Nowak for their willingness to discuss about this research topic. I am also greatful to Dr. Suinn Park, Dr. Chul Sung, Dr. Changjoo Nam, Han Wang, Shashwat Lal Das, Qinbo Li, Ankur Singhal, Kyunghoon Kim, Mitchell Priour, Amey Parulkar, and Randall Reams for listening, offering me advice, and supporting me through this process. In addition, I would like to thank all my colleagues at Texas A&M University for their kind and memorable support. Most of all, I am gratefully indebted to my wife, Heeyeon Chang, for her valuable comments, advice, and warm encouragements on this thesis. Lastly, I miss my best friend, Woosung Choi, who recently deceased. His encouragement and support will not be forgotten. May his soul rest in peace.

Part of this research was funded by National Science Foundation, under grants #905041, #1208174, and #1256086 (PI: Yoonsuck Choe).

TABLE OF CONTENTS

Page

ABSTRACT ii

DEDICATION iv

ACKNOWLEDGEMENTS v

TABLE OF CONTENTS vi

LIST OF FIGURES viii

1. INTRODUCTION 1

1.1 Motivation 1
1.2 Objective 3
1.3 Approach 3
1.4 Significance 6
1.5 Outline of the thesis 7

2. BACKGROUND AND RELATED WORK 8

2.1 Background 8
2.1.1 Knife-Edge Scanning Microscope 8
2.1.2 KESM data set 10
2.1.3 Staining method for vascular tracing 10
2.2 Related work 12
2.2.1 Seed point selection algorithms 12
2.2.2 Vector tracing-based algorithm 13
2.2.3 Skeletonization 15
2.2.4 Nissl data reconstruction 18

3. METHODS 21

3.1 Pre-processing 21
3.1.1 Image subsampling 21
3.1.2 Image triage 22
3.1.3 Region of interest extraction 23
3.1.4 Illumination artifacts correction 24

3.2 Thresholding . . . 28
3.2.1 Dynamic global thresholding . . . 28
3.2.2 Difference of Gaussian filtering . . . 30
3.3 Post-processing . . . 32
3.3.1 Partitioning the volume . . . 32
3.3.2 Noise removal . . . 33
3.4 Connecting discontinuity . . . 40
3.4.1 Connecting small discontinuity . . . 41
3.4.2 Connecting large discontinuity . . . 44

4. RESULTS AND ANALYSIS . . . 48

4.1 Reconstruction results of KESM mouse Nissl data set . . . 48
4.2 Analysis . . . 48
4.2.1 Validation of the KESM mouse Nissl data set . . . 50
4.3 Performance comparison of the proposed method against Lim's method 51
4.3.1 Small data set . . . 52
4.3.2 Large data set . . . 55

5. DISCUSSION . . . 59

5.1 Contributions . . . 59
5.2 Open issues and future works . . . 59
5.2.1 Open issues . . . 59
5.2.2 Future work . . . 61

6. CONCLUSION . . . 63

REFERENCES . . . 64

LIST OF FIGURES

FIGURE Page

1.1 Various sources of lighting irregularities. Due to knife misalignment, overall uneven illumination artifacts are exhibited along the x-axis. The two white arrows represent visible streaks due to knife defects. Adapted from [1]. 2

1.2 The left panel shows the volume visualization from mouse India ink data while the right panel shows the volume visualization from rat Nissl data. Adapted from [1]. 4

2.1 Detailed illustration of KESM: (1) high-speed line-scan camera, (2) microscope objective, (3) diamond knife assembly and light collimator, (4) specimen tank , (5) three-axis precision air-bearing stage, (6) white-light microscope illuminator, (7) water pump for the removal of sectioned tissue, (8) PC server for stage control and image acquisition, (9) granite base, and (10) granite bridge. Adapted from [2]. 9

2.2 Imaging principle of the KESM. Adapted from [2]. 10

2.3 Various types of volume visualization of the KESM mouse India ink data set. (a) Raw data volume (b) initial thresholding (c) sagittal view (d) coronal view (e) horizontal view (f) local 3D volume in close up view (g) a single coronal section (h) overlaid version of the 20 coronal sections. Adapted from [2]. 11

2.4 Overview of the tracing procedures. (a) Direction detection along y-axis. (b) Calculating three local axis lengths to adjust the center point for tracing. (c) Estimating the local MIP volume based on medium axis length. (d) Local MIP and 2D tracing results. (e) Evaluation and adjustment on the vascular direction in 3D context using the Hessian matrix. Adapted from [3]. 14

2.5 Tracing with the flat box. Surface S_i of the flat box is placed based on the seed point position. Also, the predicting window is placed on the opposite side of surface S_{i+1} along the vascular network, which is the tracing direction. The centroid of the vessel cross section in the predicting windows is determined to be the next candidate point. Step size is the distance between S_i and S_{i+1} of the flat box. Adapted from [4]. 16

2.6 Volume visualization of duplicated tracing results using Yang's MFB method [4]. Redundant centerline tracing is a serious problem of MFB. White centerlines are duplicated. 17

2.7 Principle of the skeletonization algorithm. Adapted from [5]. 17

2.8 Error-prone results of the skeletonization algorithm. Although skeletonization is useful and easy to apply to any data set, contour deformation of the skeletal representation is a serious issue. Yellow dots represent a misleading branch caused by the contour deformation in the skeletonization algorithm. 18

2.9 Principle of Lim's method (guidance map) to remove the binarization artifact. It removes the connected components that are not vertically replicated in the two consecutive images. Adapted from [6]. 20

2.10 Volume visualization of the KESM partial rat Nissl data set by Lim's method. The part marked in yellow shows noisy part of the volume incorrectly identified as vasculature. Adapted from [6]. 20

3.1 Workflow of pre-processing 21

3.2 (a) shows the raw image of the mouse Nissl image. (b) shows the generated freehand mask (c) shows the ROI after applying the freehand mask. 24

3.3 Homomorphic filtering, which is most commonly used for illumination correction. 25

3.4 Example of homomorphic filtering on the KESM mouse Nissl image. Illumination artifacts across the image were greatly reduced (inside the yellow circle). 26

3.5 Iterative results after applying anisotropic diffusion filtering on the KESM mouse Nissl data set. As a result, anisotropic diffusion diffuses less over regions where the gradient magnitude is large, whereas it diffuses more over regions where the gradient magnitude is small. . . 27

3.6 Workflow of thresholding 28

3.7 Defining a dynamic threshold value of the image. m represents the mean value and T represents threshold value of the image. 30

3.8 (a) shows the raw image of the mouse Nissl image. (b) shows the segmented image of the mouse Nissl image after applying the dynamic global thresholding method. Within the red circles are vessel cross sections. 31

3.9 Example of DoG processing. This figure shows all high contrast blobs are segmented. Red circle indicates the vessel cross section. Note that all high-contrast objects (i.e. white binarized blobs) will be processed in the post-processing step in order to eliminate noise results. 31

3.10 Workflow of post-processing 33

3.11 After initial thresholding. Discriminating each CC as a noise or vasculature is hard in the 2D context. 34

3.12 (a) shows the projected image of the 3D volume to the X-Y (2D) plane before noise removal. (b) shows the extracted component of the streaks that are projected into the X-Y plane. (c) shows the are extracted components of the 3D volume that are less than the threshold value. (d) shows the final results. 35

3.13 A block diagram of the ANN. We use 17 local geometric properties as input and 50 neurons as hidden layers. The outputs are scaled values that could be determined as vasculature or noise. The local geometric properties used as input were (1) major axis length, (2) first axis length, (3) second axis length, (4) third axis length, (5) meridional eccentricity (i.e. the eccentricity of the section through the longest and the shortest axes), (6) equatorial eccentricity (i.e. the eccentricity of the section through the second longest and the shortest axes), (7) area, (8) max intensity, (9) mean intensity, (10) standard deviation of each CC's intensity, (11) surface 3D, (12) surface 3D density, (13) surface 3D density estimate, (14) mean breadth (i.e. the mean breadth of the labeled CC), (15) mean breadth estimate (i.e. the estimate of mean breadth within the labeled CC), (16) mean breadth (i.e. the ratio of mean breadth over volume of the CC), and (17) euler 3D (i.e. the Euler number of the labeled CC). For the target output, the human labeled results as vasculature or noise were provided. 39

3.14 Mean-Squared Error of the ANN 40

3.15 The left panel shows the sagittal view of the raw images. The right panel shows the sagittal view of the initial thresholding result. Yellow bounding boxes indicate the location of a small discontinuity 41

3.16 Example of connecting small discontinuity. Note that only B_n is empty among the four consecutive bounding boxes, but the others are filled with at least one pixel in the bounding box. B_n, will be replaced with a new image, the union of B_{n-1} and B_{n+1}. In this case, B_{n+2} will not be influenced by B_n. 42

3.17 Example of connecting small discontinuity. Note that two bounding boxes, B_n and B_{n+1}, are empty. Thus, B_n and B_{n+1} will be replaced with a new image, the union of B_{n-1} and B_{n+2}. 43

3.18 Example of connecting small discontinuity. Note that B_{n+2} from L_{n+2} is empty. In this case, L_{n+2} will not be filled with any pixel since subsequent bounding box of L_{n+2} does not exist. 43

3.19 Top and bottom centroids in the connected component 44

3.20 The left panel shows an example of large discontinuity. The right panel shows how to find the minimum Euclidean distance between the CCs. 45

3.21 If there is a discrepancy between the initial centroid that are extracted from the 2D images and the predicted centroids (e.g. (x_2,y_2), (x_3, y_3), ..., (x_{n-1}, y_{n-1})), the bounding box of the predicted blob will be shifted. The location of the bounding box will be automatically adjusted once it reaches the end of the CC. 46

3.22 The left panel shows a sagittal view of the 3D volume with two disconnected components. The right panel shows a sagittal view of the 3D volume where two components are successfully connected by the proposed method. 47

4.1 Volume visualization of the KESM mouse Nissl data. The left panels show different viewing angles of the initial thresholding results. The right panels show different viewing angles of the processed volume after noise removal. 49

4.2 This block diagram shows the reconstruction workflow for the KESM rat Nissl data set. We selectively applied methods from the proposed method for the KESM mouse data. Note that ROI extraction and ANN were not utilized here. 52

4.3 (a) shows the stack of the ground truth images (200 voxels × 200 voxels × 200 voxels). (b) shows the stack of the generated images by Lim's method. The right panel has frequent discontinuities but in the left panel they are connected (red circles). 53

4.4 (a) shows the stack of the ground truth images (200 voxels × 200 voxels × 200 voxels). (b) shows the stack of the generated images by the proposed method. Although we generated ground truth by a human operator, contrasts of some regions were quite ambiguous that led to several discontinuities. However, the proposed method overcame such issues (blue circles). 53

4.5 Comparison of Lim's method and the proposed method 54

4.6 Comparison results of the volume projection (binarized) into X-Y plane (2D). The left image shows the volume that is reconstructed by Lim's method. The right image shows the volume that is reconstructed by the proposed method. 54

4.7 Anterior view of the results of Lim's method compared to those of the proposed method. ParaView 4.1.0 64-bit [7], a 3D visualization framework, was used to visualize the data. Inside of the yellow circle, the left panel shows lots of noise, whereas the right panel shows that the noise has been removed. 55

4.8 Posterior view of the results from Lim's method and the proposed method. Inside the yellow circle, the left panel shows lots of noise, whereas the right panel shows that the noise has been removed. . . . 56

4.9 Close up comparison between Lim's method and the proposed method 57

4.10 Figure (a) and (c) are log scale histograms that indicate the number of CCs in each volume as a function of CC length. The X-axis represents the centerline length of CC, and the Y-axis represents the number of CC in the volume (log scale). Figure (b) and (d) are frequency histograms that indicate the number of CCs with L>1000 for the two methods. 58

5.1 The left panel shows a coronal section from the Mouse Brain Architecture Project at Cold Spring Harbor Laboratory [8]. The right panel shows a coronal section from a KESM mouse India-ink data set. . . . 61

5.2 The left panel shows the volume visualization of a vascular network. The right panel shows the volume visualization of cell bodies and the vessels in the same volume. Adapted from [9]. 62

1. INTRODUCTION

1.1 Motivation

The relationship between cerebral blood flow and neuronal activity plays an important role in understanding brain diseases [10]. For example, in Alzheimer disease, cerebral vascular reactivity is decreased resulting in vascular dysfunction [11]. In ischemic stroke, oxygen free radicals are generated between the microvessels and the brain tissues resulting in cell damage [12]. These studies show that investigating neurovascular networks can lead to a breakthrough in understanding macro and microcirculation and their influences on brain disorders.

Recent developments in 3D microscopy enabled the imaging of neurovascular structures in small animal brains [13, 14, 15, 16]. By using the brain images, we can visualize and analyze neurovascular networks. Low-resolution methods like Magnetic Resonance Imaging (MRI) provide an overview of major structural and functional brain architecture [13, 14]. On the other hand, high-resolution methods like Serial Block-Face Scanning Electron Microscopy (SBF-SEM) enable us to look into detailed microstructures in very small volumes [13].

However, both methods have limitations in imaging a whole brain. Low resolution methods such as functional magnetic resonance imaging (fMRI) is capable of imaging large-scale volume, but it gives a coarse voxel resolution (e.g. voxel size 3mm $\times$ 3mm $\times$ 3mm [17]). High-resolution methods such as Serial Block-Face Scanning Electron Microscopy (SBF-SEM) provide images of nanoscale resolution, but it only allows us to look at very small volumes [1]. Thus, these two modalities are not capable of whole brain scale imaging for analyzing neurovascular networks.

Knife-Edge Scanning Microscopy (KESM) is a high-throughput and high-resolution

technique that images blocks of tissues using physical sectioning, which bridges the gap between the lower resolution large volume method, and the higher resolution small volume method [18]. The KESM can image whole mouse brain volumes at a submicrometer voxel resolution (voxel size 0.6μm $\times$ 0.7μm $\times$ 1μm) [19], and the KESM has successfully imaged whole mouse brain that stained in Nissl [20], Golgi [21], and India ink [22]. The KESM Nissl data contain significant details of cell nuclei of neuronal and glial cells because Nissl stain labels the nucleic acid contents of the cells, including endoplasmic reticulum, ribosomes, and the cell nuclei [23], whereas the vessels remain unstained. Through the KESM Nissl data, we can see the relationships between somatic cells and microvascular networks. Therefore, we expect that reconstructing microvascular networks of the KESM Nissl data will contribute to the study of the structure and function of the microvascular networks.

Figure 1.1: Various sources of lighting irregularities. Due to knife misalignment, overall uneven illumination artifacts are exhibited along the x-axis. The two white arrows represent visible streaks due to knife defects. Adapted from [1].

1.2 Objective

KESM mouse and rat Nissl data set has several challenging issues to be resolved to reconstruct the microvascular networks. There are various sources of noise present in the KESM Nissl data set, which make it hard for us to accurately reconstruct the microvascular network [13]. First, uneven illumination artifacts are present in the KESM Nissl data. Most lighting artifacts are generated by lighting irregularities of the KESM owing to knife angle, illumination power source fluctuation, and knife vibration during the sectioning of the specimen [1]. These lighting irregularities are shown as uneven illumination artifacts across the image (Figure 1.2). Second, some high-frequency streaks due to nick on the knife and ribbon boundary are present in the image. Third, the KESM Nissl data exhibit some noise due to chatter that appear as locally regular patterns in the image.

Furthermore, some unstained or low contrast vessel cross section regions of the microvascular networks (i.e. blob-like regions that are the cross section through the vessels) result in discontinuities in the reconstructed volume (Figure 1.2). Due to the nature of the microvascular networks, all vascular segments should be connected to each other to allow blood to flow through the vasculature [1]. In this thesis project, we aim to reconstruct neurovascular networks from whole-brain KESM mouse Nissl data by applying a novel automated method.

1.3 Approach

To automatically reconstruct the microvascular networks from the KESM mouse and rat Nissl data, we developed a novel method. The method consists of (1) pre-processing, (2) thresholding, and (3) post-processing steps.

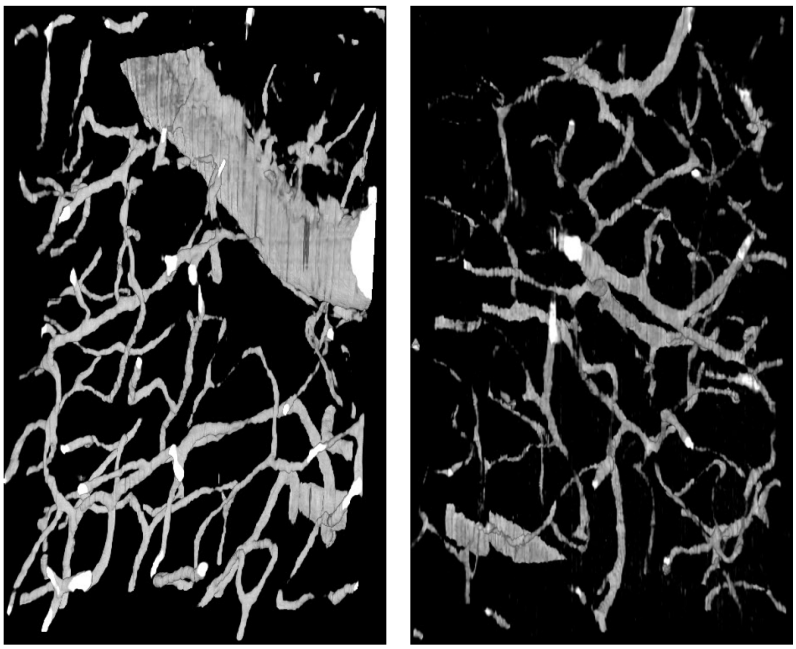

Figure 1.2: The left panel shows the volume visualization from mouse India ink data while the right panel shows the volume visualization from rat Nissl data. Adapted from [1].

In the pre-processing step, we excluded severely corrupted images due to several system malfunctions that could happen at the positioning stage, line scan camera, lightning path, diamond knife, and the pump [24]. After that, the KESM Nissl data were subsampled to reduce computation time. With these image sections, we extracted the boundary of the brain surface defining a region of interest (ROI) using freehand masks. Due to multiplicative illumination artifacts reside in the low-frequency domain, we used homomorphic filtering to block the low frequencies by high-pass filter of homomorphic filtering. Also, we adopted anisotropic diffusion filter to suppress high-frequency details while preserving edges and lines.

In the thresholding step, the proposed method was designed to extract all possible vessel cross sections from the image data in the 2D context. It is difficult to determine a local threshold value of the vessel cross section due to lack of prior

knowledge of certain characteristic of the vessel cross sections. Thus, we used global thresholding method based on a mean value of the image. Each threshold value of the image was determined separately. However, defining threshold values of the cerebellum region was difficult using global thresholding, since different characteristics and features resided in the cerebellum region. Therefore, we locally segmented the vessel cross section in the cerebellum region using Difference of Gaussian (DoG) filter because the pixels of the cerebellum regions had more high-frequency data than other regions. After the thresholding step, the processed sections exhibited several noise features. Therefore, we also had to discriminate the vascular networks from the noise features.

The main purpose of the post-processing step is to extract the vascular networks by suppressing various sources of noise in the reconstructed 3D volume. The proposed method examined the connected component (CC) in the 3D context instead of 2D. This is because the vasculature has a coherent structure in the 3D context while noise tends to appear randomly across the image. However, 3D volume analysis requires large amount of memory. Hence, we partitioned the volume into subvolumes. After partitioning the volume, each subvolumes were processed independently. Then, these subvolumes were merged into a single volume once the post-processing is done. In the 3D volume of the reconstructed image, we found two types of noise; streaks due to nick on the knife and ribbon boundary, and noise due to chatter. At first, streaks were removed through the following process: (1) Project the volume to a 2D (X-Y) plane; (2) apply automatic global thresholding algorithms such as Otsu, H-maxima, and mean-based thresholding to the projected image; (3) calculate regional property of each CC, and extract the CC if the CC was determined as the streaks that have certain angles and ratio of eccentricity; and (4) retrieve the X-Y coordinates of the pixels that are extracted from the CC, and set the value of

the pixels to zero. Furthermore, to remove the noise due to chatter, we measured centerline length along the axial direction. We eliminated the CC if the length of the CC is less than the threshold value that was empirically estimated. Although several noise components were removed through the previous noise removal process, some noises were still present. Thus, we adopted artificial neural networks (ANN) at the end of the post-processing step. As an input vector of the ANN, we used three-dimensional regional properties, and a hidden layer with 50 neurons empirically determined through cross-validation. Input data were all CCs found from the previous noise removal process. The output of the ANN was a binary value that indicates a vascular object or noise. The proposed method also connected discontinuities between the CCs in the 3D context; small and large discontinuities. The proposed method attempted to fill in the small discontinuities if one or two empty disconnected cross sections existed in each of the four consecutive sections. On the other hand, in case of large discontinuities along the z-axis, the proposed method measured the Euclidean distance between the CCs. If the distance between the CCs is less than the threshold value, which was empirically determined prior to the process, the proposed method automatically connected the large discontinuity.

1.4 Significance

This thesis project introduces an novel automated method to reconstruct the vascular networks. Most previous works that have been done in Brain Networks Laboratory (BNL) only processed a small scale volume ($\sim$ 500 voxels $\times$ 500 voxels $\times$ 500 voxels with a voxel size of 0.6μm $\times$ 0.7μm $\times$ 1μm). In this thesis, we successfully processed whole-brain scale mouse data. To process the whole-brain data set,

the proposed method automatically partitioned the image volume into subvolumes in order to fit each volume size into available memory. In addition, the proposed method is optimized to matrix operation, which considerably reduces the processing time and increases the throughput. Furthermore, we proposed a noise-robust framework that is globally applicable to other image data sets. In sum, the proposed method provides fast and accurate reconstruction results, offering accurate analysis on its anatomical statistic.

1.5 Outline of the thesis

In chapter 2, this thesis will briefly introduce the Knife-Edge Scanning Microscope (KESM), characteristic of the KESM data sets, and methods for staining blood vessels. Also, this thesis will illustrate several related works regarding seed point selection, vector tracing algorithm, skeletonization, and Nissl data reconstruction. In chapter 3, this thesis will present various image processing techniques in pre-processing, thresholding, and post-processing step. In chapter 4, we will see experimental results as well as quantitative analysis. Lastly, in chapter 5, this thesis will address open issues and future works. In chapter 6, the conclusion of the thesis will be presented.

2. BACKGROUND AND RELATED WORK

2.1 Background

2.1.1 Knife-Edge Scanning Microscope

Nowadays, various types of whole-brain scale imaging methods have been developed. Magnetic Resonance Imaging (MRI) allows us to see an overview of whole-brain-scale structure and function, but at a low resolution. However, reconstructing detailed cellular circuits or individual fibers is not feasible since MRI provides a relatively low voxel resolution (e.g. MRI approaches at most 156μm voxel resolution [25]). On the contrary, Electron Microscope (EM) enables us to look into microstructures, providing nano-scale voxel resolution. However, EM is also not adequate for large scale or deep-tissue imaging.

In this section, we introduce Knife-Edge Scanning Microscope (KESM). The KESM was initially designed by Bruce H. McCormick and developed by the Brain Network Laboratory (BNL) at Texas A&M University. KESM is a high-throughput imaging method providing a high-resolution image, and bridges the gaps between high resolution imaging technique with a small volume (e.g. EM) and low resolution imaging technique with a large whole-brain volume (e.g. MRI). KESM has been used to image whole mouse brains with different staining methods at submicrometer resolution: Golgi, India ink, and Nissl staining method. Figure 2.1 illustrates the major components of the KESM.

As shown in Figure 2.1, the three-axis air-bearing stage is operated to provide accurate mechanical movement for X- and Y-axis with encoder resolutions of 20nm, and vertical z-axis with resolutions of 25nm [26], which provides robust registration of the KESM. One of the distinctive features of the KESM is the knife-collimator

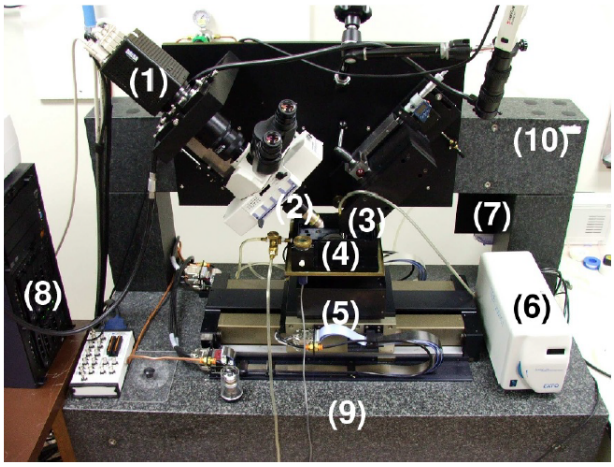

Figure 2.1: Detailed illustration of KESM: (1) high-speed line-scan camera, (2) microscope objective, (3) diamond knife assembly and light collimator, (4) specimen tank , (5) three-axis precision air-bearing stage, (6) white-light microscope illuminator, (7) water pump for the removal of sectioned tissue, (8) PC server for stage control and image acquisition, (9) granite base, and (10) granite bridge. Adapted from [2].

assembly. The knife-collimator assembly serves a dual use; a white-light collimator for providing illumination and a diamond microtome for cutting individual sections of the specimen. The knife-collimator assembly has a diamond knife and is rigidly mounted to a granite bridge. This diamond knife is angled to be perpendicular to the optical axis of the microscope [1]. After specimens are embedded in hard polymer resin blocks, this specimen block is affixed on the positioning stage, and then the stage with the specimen is moved toward the stationary diamond knife to generate 1μm-thick sections. At the time of sectioning the specimen, line-scan imaging is done near the top of the diamond knife that generates a high-resolution image from each cut tissue. Finally, the scanned image is sent to the computer server. This whole process of the KESM gives a large stack of 2D images. Figure 2.2 illustrates detailed imaging principle of the KESM.

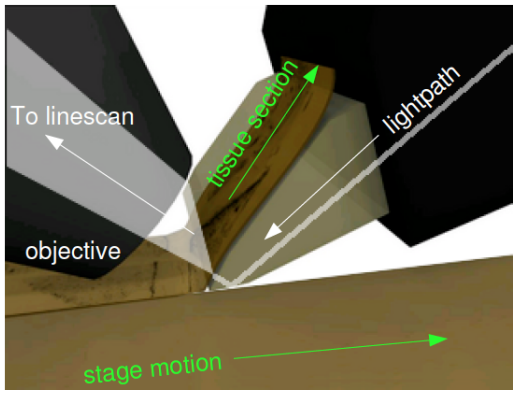

Figure 2.2: Imaging principle of the KESM. Adapted from [2].

2.1.2 KESM data set

The proposed research uses the whole mouse and partial rat brain sectioned by the KESM at a submicrometer resolution (voxel size 0.6 μm $\times$ 0.7 μm $\times$ 1.0 μm) [13]. The number of coronal sections of the whole-brain mouse Nissl images is 8,396, while the rat brain had 2,072 sagittal sections. Before we start to reconstruct the neurovascular network, we need to filter out damaged images (e.g. long streaks and large smear) caused by system malfunction of the KESM [27]. The damaged image could degrade the quality of the reconstructed volume that leads to the generation of error-prone results. Therefore, we manually excluded the damaged images from the Nissl data set.

2.1.3 Staining method for vascular tracing

To analyze the vascular networks, we need to reconstruct the geometry of the vasculatures. India Ink and Nissl staining are generally used for investigating the vascular networks. India ink staining method only dyes the vessel black by perfusing

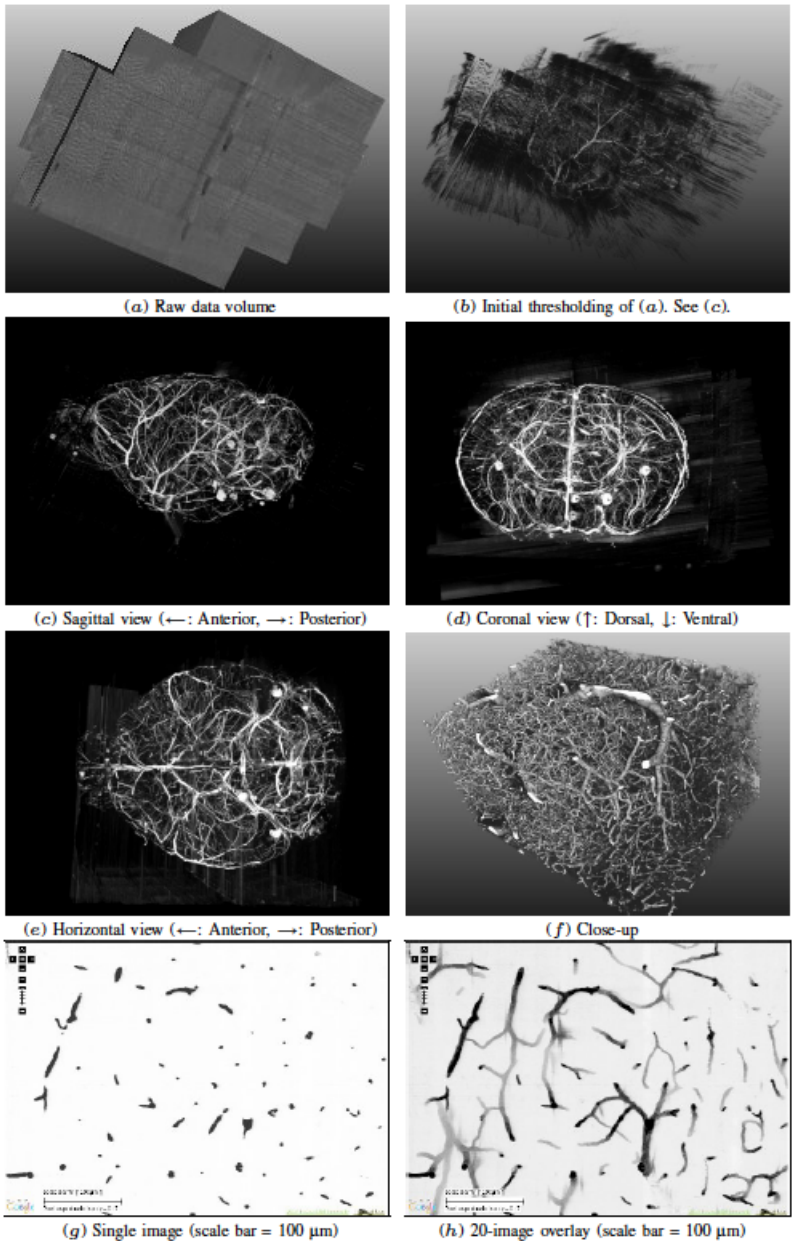

Figure 2.3: Various types of volume visualization of the KESM mouse India ink data set. (a) Raw data volume (b) initial thresholding (c) sagittal view (d) coronal view (e) horizontal view (f) local 3D volume in close up view (g) a single coronal section (h) overlaid version of the 20 coronal sections. Adapted from [2].

India ink through the circulatory system [13]. Thus, India ink data clearly show vessel structures although it does not show any surrounding cell nuclei of neuronal or glial cells (Figure 2.3). In comparison, Nissl staining method stains the nucleic acid contents of cells including endoplasmic reticulum, ribosomes, and the cell nuclei while the vessels remain unstained. Therefore, Nissl data provide not only the vessel information but also their surroundings cells, simultaneously. However, extracting vessels from the Nissl data is relatively difficult since the data contain various cellular features.

2.2 Related work

2.2.1 Seed point selection algorithms

Shan et al. [28] proposed a seed point selection method on ultrasound images. At the beginning, they adapted the region growing algorithm, which is a popular segmentation method for ultrasound image processing, to select the seed point within the breast lesion. Most region growing methods require manual selection to set the seed points, but Shan et al. implemented automatic seed point selection for the region growing. First, they used anisotropic diffusion filter in order to suppress image noise and preserve edges. Then, they iteratively applied a heuristic method to find a reasonable threshold by analyzing the characteristics of the breast lesion of every connected component. Specifically, if none of the connected component intersects with the local window (image center region) that is approximately half the size of the whole image, the current local minimum in the image is determined as the threshold value. This process continues until the connected component intersects with the center region of the whole image. After that, Shan et al. eliminated the boundary-

connected region of the breast lesion by applying the same technique in the threshold selection step above. Next, Shan et al. ranked the remaining region by measuring the regional properties (e.g. distance and area of the breast lesion). Finally, the highest scored region was selected as the seed point. Although Shan et al.'s method automatically selects the seed points, it is not feasible to apply to other data because the implemented method involves many heuristic that can be only applicable to the specific data set they used.

Xiao et al. [29] implemented an automatic algorithm called adaptive geometrical vessel tracking (AGVT). They adopted Hessian matrix that is generated from a ridge enhancement image data set, which is initially obtained by suppressing background noise and enhancing vessel cross sections. Subsequently, seed points were automatically selected if local maxima are higher than the other pixel values. Therefore, the pixel that is lower than the threshold value, determined by the Hessian matrix, was removed. After that, direction determination was conducted. Note that the selected points could be continuously adjusted along the centerline points. However, we should consider that determining the Hessian matrix is computationally expensive, and this method does not consider normalizing uneven illumination artifacts that could be present in certain data sets. Hence, AGVT could not be applicable to other data set.

2.2.2 Vector tracing-based algorithm

Han et al. [3] developed a robust and fast filament-tracing algorithm for both 2D and 3D data sets. For 2D tracing, they applied a heuristic algorithm in order to determine the direction of the vessel trace using a Moving Window (MW). Fur-

thermore, they implemented Cubic Tangential Trace Spline (CTTS) to enhance the robustness of the branch detection during traversing with the MW. The idea of MW and CTTS were extended to develop a method based on local maximum intensity projection (MIP) for 3D vascular tracing. Han et al. limited the size of the MIP cube to get an uncluttered projection. However, the MW method is not feasible to process a large scale volume since each iteration in local volume requires complex computation (e.g. processing time of 128 voxels $\times$ 128 voxels $\times$ 128 voxels requires approximately 200 seconds). Furthermore, a human operator should manually select the seed points in the beginning. Figure 2.4 illustrates the principals of Han et al.'s method.

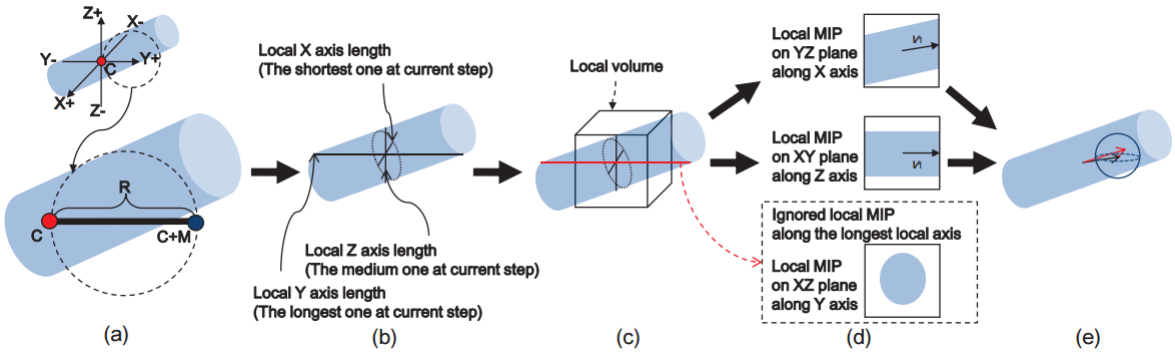

Figure 2.4: Overview of the tracing procedures. (a) Direction detection along y-axis. (b) Calculating three local axis lengths to adjust the center point for tracing. (c) Estimating the local MIP volume based on medium axis length. (d) Local MIP and 2D tracing results. (e) Evaluation and adjustment on the vascular direction in 3D context using the Hessian matrix. Adapted from [3].

Yang [4] introduced a fast fiber tracing method called Moving Flat Box (MFB) (Figure 2.5). The principal of the moving flat box is similar to the MW algorithm, but it overcomes the shortcoming of MW; taking excessive time. First, Otsu's threshold method [30] was applied to binarize all image layers, and then seed points were

automatically selected from each center point of the vessel cross section which were located on all surfaces of the 3D volume. This method only explored adjacent pixels of the vessel cross section in a different plane (i.e. z-axis) instead of finding every pixel within the 3D volume. Subsequently, MFB traced the center point starting from the seed point to the next centroid of the cross section as a next candidate point of the moving trajectory. The processing in MFB is much faster than MIP since MFB only requires the top and the bottom surfaces of the MFB to trace the vessel cross sections while MIP requires six surfaces. However, MFB has a drawback: similar trajectories of duplicated centerlines are traced during the traversal of the 3D volume. This is because the similar centerlines could be traced multiple times due to the multiple seed points on different surfaces in the 3D volume [4]. As a result, duplicated tracing results with different tracing directions exist in the 3D volume (Figure 2.6.a). Moreover, MFB is occasionally not well fitted to the vessel cross section during traversal, resulting in an inaccurate center point detection, which eventually leads to error-prone centerline tracing.

2.2.3 Skeletonization

Singhal [5] adopted skeletonization-based tracing algorithm (Figure 2.7) to trace the vasculature. He extracted the skeleton of the vasculature from the raw image by iteratively eroding a pixel until no further topological change occurs in the image, which is called morphological thinning. The skeletonization algorithm yields unnecessary branches that are caused by small perturbations near the boundary of the reconstructed vasculature. Figure 2.8 shows the significant error of branch point after applying the skeletonization method.

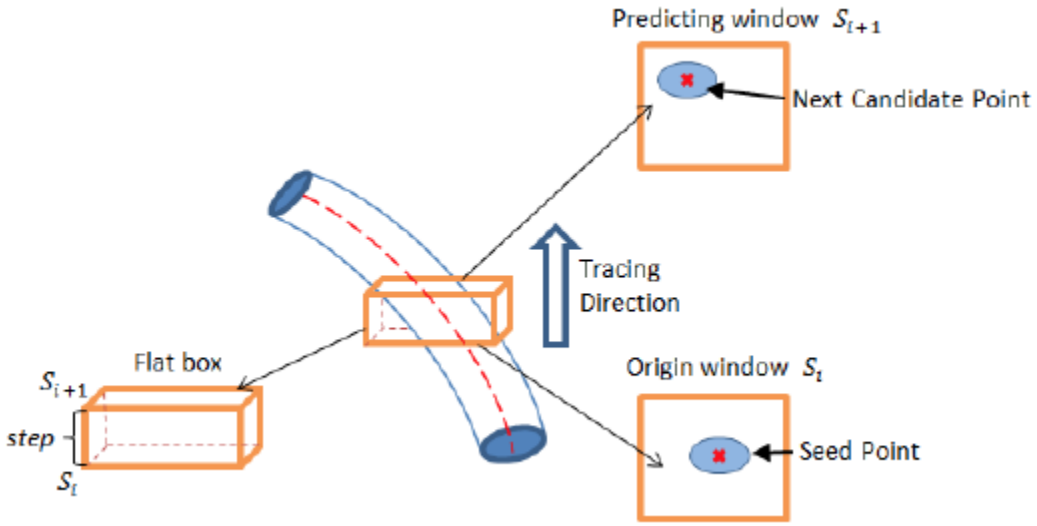

Figure 2.5: Tracing with the flat box. Surface S_i of the flat box is placed based on the seed point position. Also, the predicting window is placed on the opposite side of surface S_{i+1} along the vascular network, which is the tracing direction. The centroid of the vessel cross section in the predicting windows is determined to be the next candidate point. Step size is the distance between S_i and S_{i+1} of the flat box. Adapted from [4].

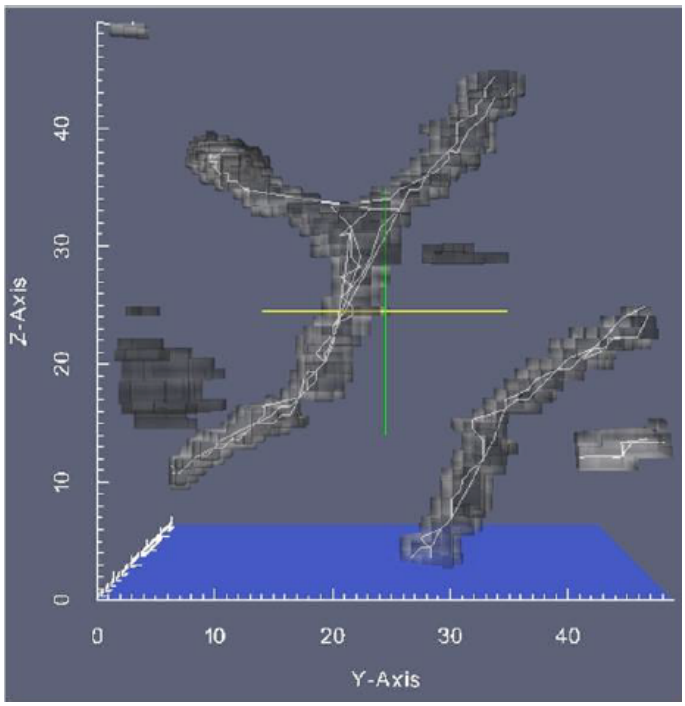

Figure 2.6: Volume visualization of duplicated tracing results using Yang's MFB method [4]. Redundant centerline tracing is a serious problem of MFB. White centerlines are duplicated.

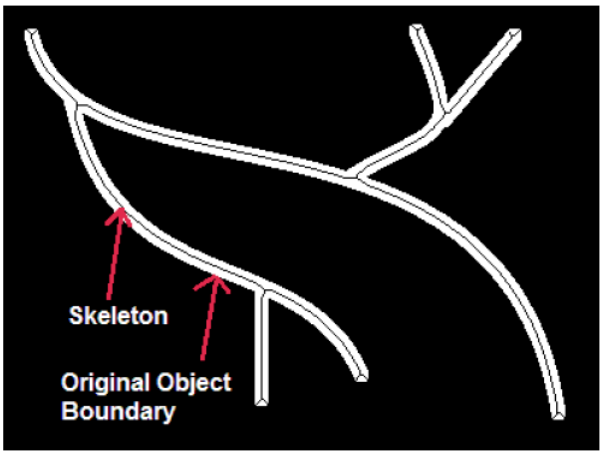

Figure 2.7: Principle of the skeletonization algorithm. Adapted from [5].

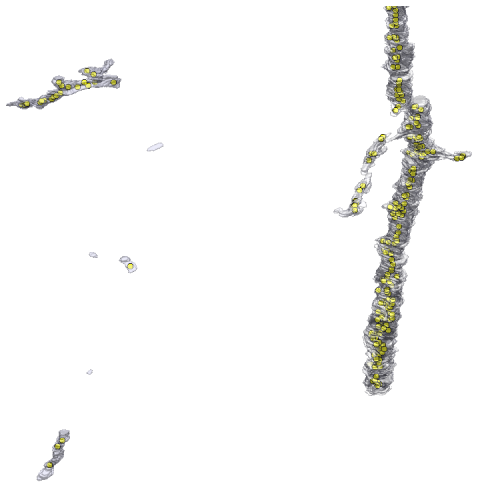

Figure 2.8: Error-prone results of the skeletonization algorithm. Although skeletonization is useful and easy to apply to any data set, contour deformation of the skeletal representation is a serious issue. Yellow dots represent a misleading branch caused by the contour deformation in the skeletonization algorithm.

2.2.4 Nissl data reconstruction

Previous works, described in section 2.2.2 to 2.2.3, were developed for small volumes of KESM India-ink data. However, KESM Nissl data sets have various types of features including imaging artifacts that need to be processed prior to extracting the desired feature (i.e. the vasculature). That is, the most techniques for reconstructing the KESM India ink data set will not be applicable to KESM mouse and rat Nissl data sets.

Lim [6] proposed an automated algorithm to trace vascular networks on KESM rat Nissl data. Lim's method consists of (1) image enhancement, (2) image binarization, (3) correcting uneven illumination correction, (4) bilevel thresholding, (5) hole filling, and (6) tracing vasculature. For removing illumination artifacts, Lim's method was designed to subtract the averaged image of whole 2D stacks from every image since most lighting artifacts appear in a number of subsequent images.

This idea is widely used to alleviate background artifacts, but it is not applicable when each layer has different illumination artifact chracteristics. For global thresholding, Lim's method adopted the maximum entropy algorithm [31] to identify the vessel cross sections. However, the maximum-entropy algorithm is efficient only if the contrast difference between a region of interest and its surrounding structure is obviously distinguishable. In other words, maximum-entropy algorithm gives rise to poor segmentation performance when all features do not have distinctive contrast. Such a poor segmentation causes erroneous outcome of the reconstruction, and frequent discontinuities in the traced vasculatures. To overcome these issues, Lim generated an intermediate image using the minimum of two consecutive images to remove erroneous binarization results. In detail, the intermediate image is computed as the minimum of two consecutive images: min (I_x, I_y) where I_x and I_x are adjacent images along the z-axis. This intermediate image is called the guidance map (Figure 2.9).

However, this simple heuristic is not robust to background noise, resulting in inaccurate segmentation because the guidance map only compares the previous and the subsequent image, not the whole connected component in the 3D volume (Figure 2.10). Moreover, this simple heuristic is not capable of connecting the discontinuity due to missing data. It only removes the connected components that are not vertically adjacent from two subsequent images. To obtain more precise results, we need to consider a whole coherent structure in a 3D context.

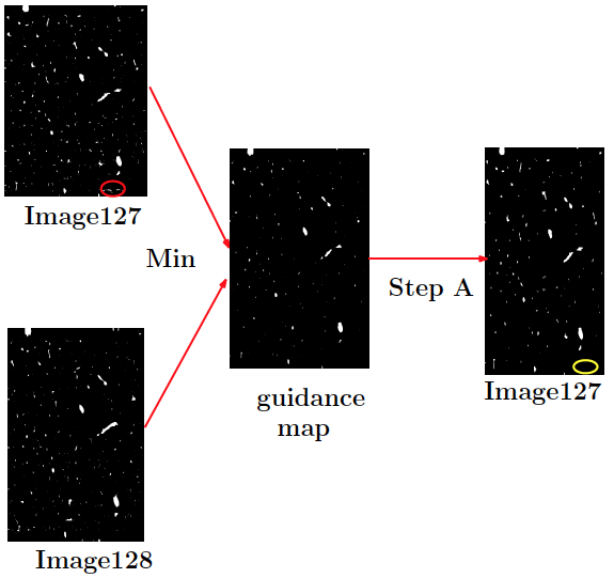

Figure 2.9: Principle of Lim's method (guidance map) to remove the binarization artifact. It removes the connected components that are not vertically replicated in the two consecutive images. Adapted from [6].

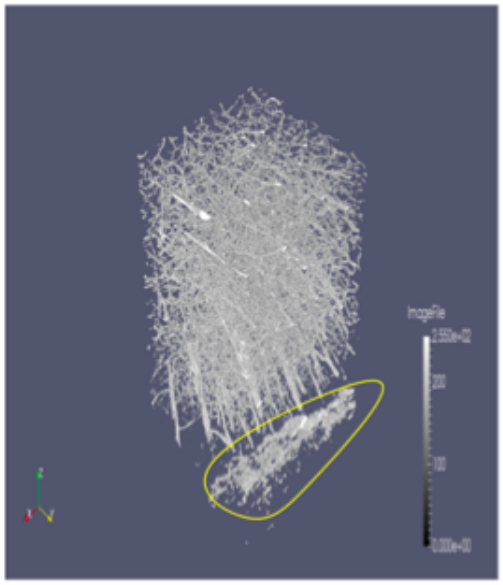

Figure 2.10: Volume visualization of the KESM partial rat Nissl data set by Lim's method. The part marked in yellow shows noisy part of the volume incorrectly identified as vasculature. Adapted from [6].

3. METHODS

3.1 Pre-processing

In this section, we introduce the pre-processing procedures. First, image subsampling is utilized to reduce the computational overhead. Second, some severely corrupted images are removed from the image stack before applying the proposed method. Third, for each layer the region of interest are extracted by free hand masks. Finally, homomorphic and anisotropic diffusion filtering techniques are employed to alleviate the imaging artifacts. Figure 3.1 illustrates the pre-processing pipeline.

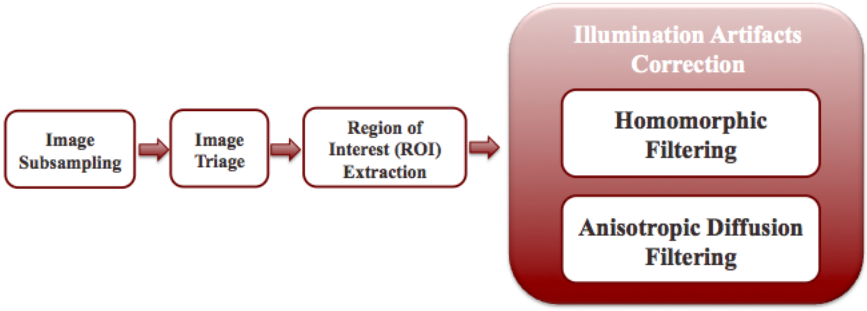

Figure 3.1: Workflow of pre-processing

3.1.1 Image subsampling

The size of the KESM whole-brain data set is approximately 2TB [13], uncompressed, so it cannot easily fit in the main memory of modern desktop computers, and it takes enormous processing time. For this reason, we need to subsample the data set so that it can fit in the main memory and can be processed quickly. However, excessive image subsampling will degrade the quality of the image. In this respect,

we manually checked the subsampled results with different ratio of the volume size in order to find a scaling factor that can subsample the original volume without data loss. First, Imagemagick, a free opensource software for command-line image manipulation, was employed to subsample the cross sections down to 50%. Second, every other cross section in the image sequences was discarded. The result was 50% of the original volume (10,000 voxels $\times$ 5,000 voxels $\times$ 8,396 voxels) thus giving us 5,000 voxels $\times$ 2,500 voxels $\times$ 4,198 voxels.

3.1.2 Image triage

A number of images have been severely corrupted due to the following: (1) nick on the diamond knife and ribbon boundary, (2) illumination interruption by dysfunction of the illumination device or obstruction on the path of the illumination, and (3) file system errors that prevent images from being written to the storage device [24]. To avoid erroneous reconstruction of the KESM Nissl data sets, we should exclude the severely corrupted images. We classified coronal sections into two categories; (1) severely corrupted image (i.e. more than 50% of the single cross section is corrupted) and (2) partially corrupted image (i.e. less than 30% of the single cross section is corrupted). We only considered the exclusion of the severely corrupted images since we anticipated that the proposed algorithm will fill missing gaps between the vasculatures. Thus, we manually excluded 243 severely corrupted coronal sections from the subsampled volume, which is 5.8% among the KESM mouse Nissl data set. The KESM rat Nissl data were relatively free of such issues.

3.1.3 Region of interest extraction

We define the region of interest (ROI) as the brain region. Note that the outside of the ROI contains no tissue and only various sources of noise, whereas the ROI contains vasculatures and the soma of the cells. Thus, extracting region of interest (ROI) is crucial to increase the accuracy of the reconstruction result as well as decrease the processing time. Possible ways to extract the brain boundary are as follows: (1) template matching, (2) mean shift clustering, and (3) freehand mask (i.e. manual segmentation).

Template matching [32] is a technique in the field of image processing to detect certain parts of the image which match the registered template. For example, we could register the certain template to train a specific pattern to discriminate the foreground (i.e. vessel features) and background (i.e. other than vessel features). In the KESM Nissl data set, however, the size and shape of the ROI varies widely across the layers, which makes it hard to employ fixed template matching.

Mean shift clustering (MSC) [33] is a popular image processing technique to aggregate regions into a coherent structure by shifting and aggregating the adjacent pixels. MSC can extract the inside of the mouse brain boundary, but it is computationally expensive. Theoretically, extracting the ROI would be possible if we successfully extract the rough contour of the ROI using Level-set algorithm [34] after applying MSC. But excessive time would be required to extract every ROI among all the layers in the 3D volume.

In this thesis, we adopted freehand mask, manually drawn ROI. Even though rendering freehand mask for each image also requires considerable time, we found that overall topology of the image sequences have no sudden change for up to 20 layers. Thus, we generated 211 freehand masks for every 20 consecutive images. Each

(a) Raw image (b) ROI boundary (c) Segmented image

Figure 3.2: (a) shows the raw image of the mouse Nissl image. (b) shows the generated freehand mask (c) shows the ROI after applying the freehand mask.

generated freehand mask was applied to 20 the consecutive layers to extract the brain region. Note that image enhancement and thresholding process were globally applied to the image after the ROI extraction. If steepness of the difference between the boundary of the ROI is greater than that between the boundary of vessel cross sections in the ROI, the proposed method may not correctly segment the vessel cross sections. In order to minimize the gradient difference between the outside and the inside of the ROI, the proposed method filled up the outside of the ROI of each coronal section with a median pixel value of the ROI of each coronal section.

3.1.4 Illumination artifacts correction

3.1.4.1 Homomorphic filtering

One of the several sources of noise in the KESM Nissl data is inconsistent illumination artifacts that are caused by misalignments between a diamond surface of the knife and the linescan camera. This misalignment led to a steady darkening in the overall illumination across the image [35]. To correct such illumination arti-

facts, we applied a homomorphic filter [36]. Generally, homomorphic filtering is used for correcting uneven illumination artifacts by removing certain characteristic of 25 multiplicative noise. Basic model of homomorphic filtering is as follows.

$$I(x, y) = L(x, y)\ R(x, y)$$

where *I(x,y)* is a 2D image, *L(x,y)* is scene illumination across the image, and *R(x,y)* is the image reflectance.

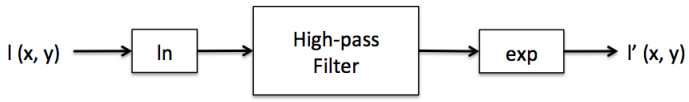

Figure 3.3: Homomorphic filtering, which is most commonly used for illumination correction.

The key task of homomorphic filtering is to remove the illumination L, but to preserves the reflectance component R. The reflectance R and illumination L can be separable by the log function. Therefore, the illumination model of the image is simply represented as follows.

$$ln(I(x, y)) = ln(L(x, y)\ R(x, y))$$
$$ln(I(x, y)) = ln(L(x, y)) + ln(R(x, y))$$

Since the illumination of the image *L(x,y)* typically resides in the low-frequency domain, high-pass filter is used to remove the log domain of L. Therefore, only log

domain of the reflectance *R(x,y)* is remained. Figure 3.3 shows the principal of homomorphic filtering, and Figure 3.4 shows the example of homomorphic filtering on the KESM mouse Nissl data set.

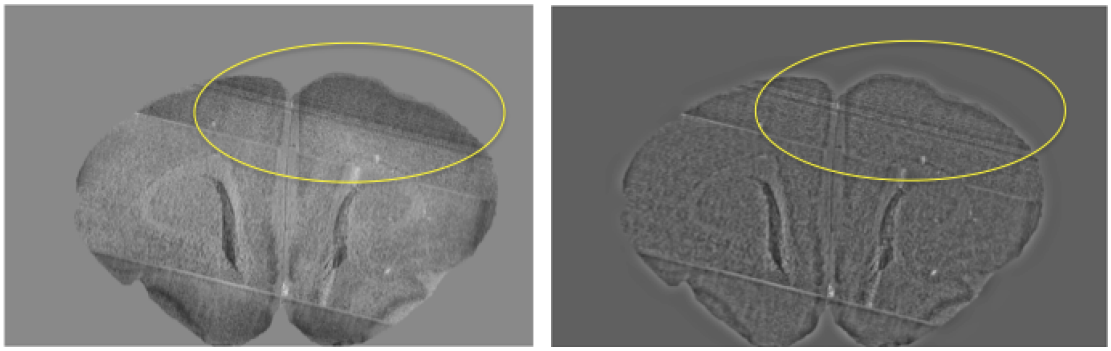

(a) Before applying homomorphic filter (b) After applying homomorphic filter

Figure 3.4: Example of homomorphic filtering on the KESM mouse Nissl image. Illumination artifacts across the image were greatly reduced (inside the yellow circle).

3.1.4.2 Anisotropic diffusion filtering

After removing the illumination artifact that resides in the log-frequency domain, we still needed to suppress high-frequency artifacts across the image. Therefore, anisotropic diffusion filter [37] was employed. Anisotropic diffusion filter is a nonlinear process, which suppresses the image noise without removing significant details such as edges and lines. It is very similar to median smoothing [36], but it is more likely to blur the entire image. The following is the description of anisotropic diffu-

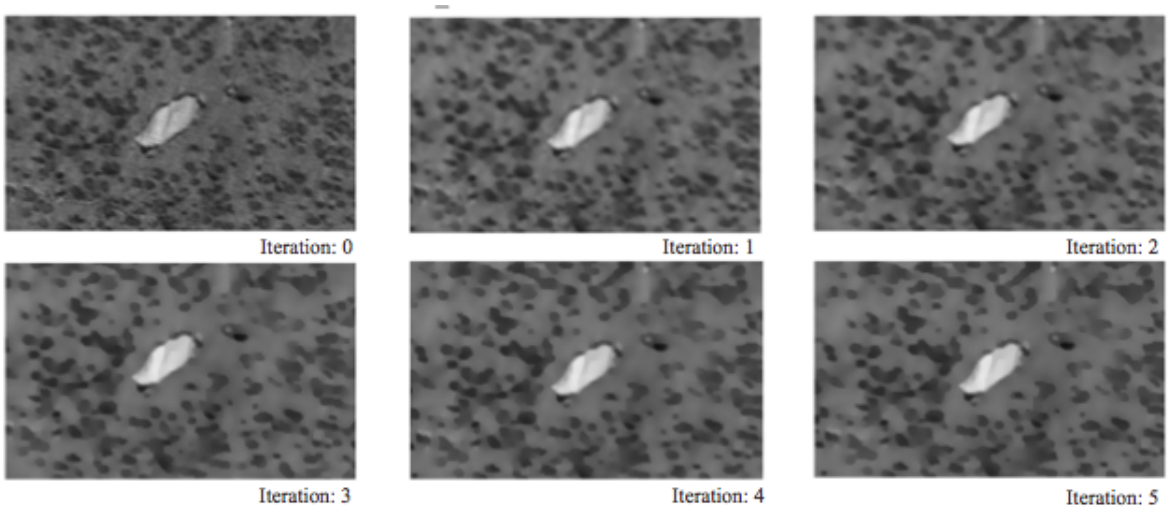

(a) Anisotropic diffusion filtering

Figure 3.5: Iterative results after applying anisotropic diffusion filtering on the KESM mouse Nissl data set. As a result, anisotropic diffusion diffuses less over regions where the gradient magnitude is large, whereas it diffuses more over regions where the gradient magnitude is small.

sion.

$$\begin{cases} \frac{\partial I}{\partial t} = div[c(||\nabla I||).\nabla I] \\ I_{t=0} = I_0 \end{cases}$$

where t is time parameter, I_0 is the image at time t, ∇I is the gradient of the image, c($||\nabla I||$) is diffusion coefficient, and div is a divergence operator.

The diffusion coefficient c($||\nabla I||$) is widely applied in two ways: The equation (1) expresses high contrast pixel values over low contrast pixel values, and the equation (2) indicates wide areas over smaller areas [37].

$$\begin{cases} c(||\nabla I||).\nabla I = exp[-(\frac{||\nabla I||}{K})^2] & (1) \\ c(||\nabla I||).\nabla I = \frac{1}{1+(\frac{||\nabla I||}{K})^2} & (2) \end{cases}$$

where k is threshold value to control smoothing level. Figure 3.5 shows the example of anisotropic diffusion.

3.2 Thresholding

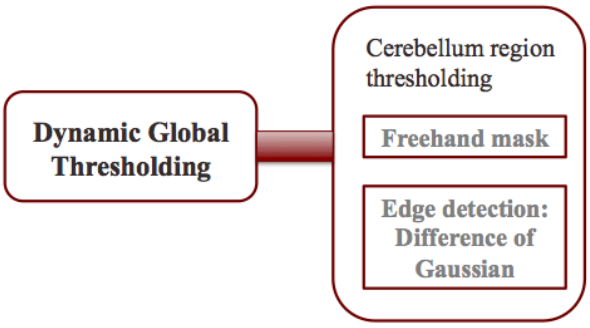

Figure 3.6: Workflow of thresholding

In this section, we initially extract the vessel cross sections from the image after pre-processing. As shown in Figure 3.6, dynamic global thresholding is used for determining the threshold value of each image. Also, difference of Gaussian filtering is employed for segmenting the vessel cross section in the mouse cerebellum region.

3.2.1 Dynamic global thresholding

This section describes a global thresholding method to extract relatively high contrast objects from the image sequences. Global and local image thresholding methods are widely used to separate pixels in an image as foreground (i.e. above a

threshold value) or background (i.e. below the threshold value) [38, 39].

Local thresholding is an effective method that adaptively determines the threshold value locally. This process helps to segment the desired objects, especially under uneven illumination. Despite the effectiveness of local thresholding, we cannot simply apply local thresholding to the KESM Nissl data because it requires significant time and resources. Moreover, the KESM Nissl data has various noise sources even though the pre-processing step partly removed the uneven illumination artifacts (low-frequency) across the image as well as some imaging errors (high-frequency). Therefore, we cannot apply the local thresholding in the KESM mouse Nissl data set due to lack of prior knowledge of the vessel cross section in the image [40].

Global thresholding only uses a single threshold value for all the image pixel to segment the desired objects. Thus, it is fast but determining the global threshold value is difficult because each image in the KESM Nissl data has the uneven illumination artifacts across the image and the imaging errors. However, we found that most vessel cross sections was likely to be located around the local maxima of the image intensity histogram, and the local maxima were mostly located above the mean pixel value of the image. Additionally, the image histogram was skewed to the left, which means a mean value of the image is the highest value among three major measures of central tendency (i.e. mean, median, and mode) (Figure 3.7). For these reasons, we dynamically calculated a mean value of each image as a threshold value. To reduce excessive removal of noise, we put a standard deviation of each image into the thresholding model. The proposed dynamic global thresholding model is as follows. The following model is the dynamic global thresholding value, T.

$$T(k) = m_k + |s_k|$$

where k is the current layer, m_k is the mean value of k-th layer, and s_k is a standard deviation of k-th layer.

As a result, all possible vessel cross sections could be segmented by the proposed global thresholding approach since we loosened the threshold value. We will discuss details regarding noise reduction and vascular extraction in the post-processing chapter. Figure 3.8 represents the results of raw image and segmented image by the proposed global tresholding method.

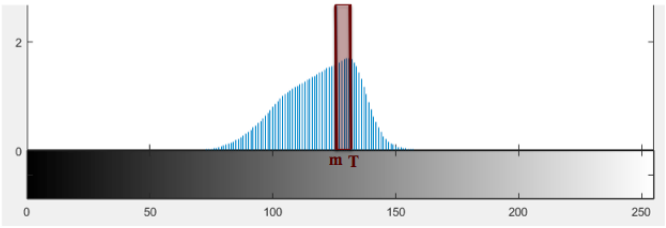

Figure 3.7: Defining a dynamic threshold value of the image. m represents the mean value and T represents threshold value of the image.

3.2.2 Difference of Gaussian filtering

As shown in Figure 3.9.(a), the pixels of the cerebellum regions have more high-frequency domains than other regions. After applying the dynamic global thresholding method in the cerebellum regions, all pixels in the region were extracted as a mixture of coherent structure and noise. The coherent structures are features of the tube-like structure. Although some noise can be shown as the tube-like structure,

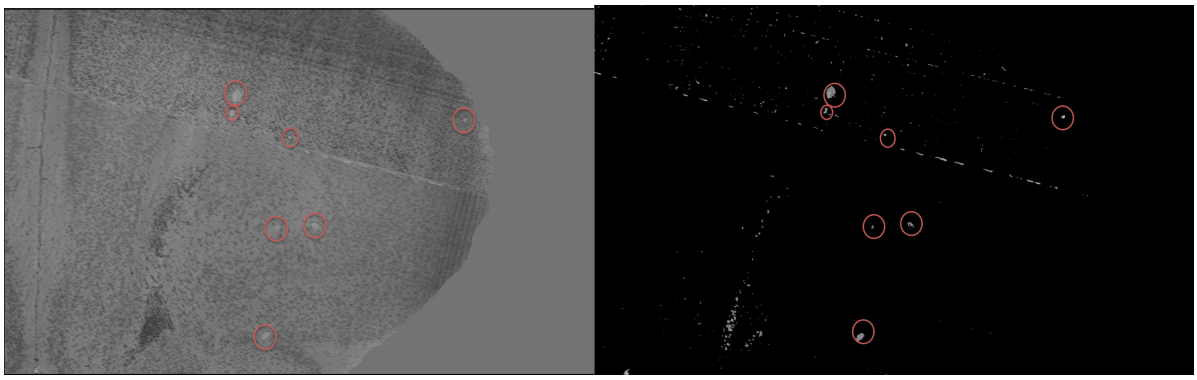

(a) Raw image (b) Segmented image

Figure 3.8: (a) shows the raw image of the mouse Nissl image. (b) shows the segmented image of the mouse Nissl image after applying the dynamic global thresholding method. Within the red circles are vessel cross sections.

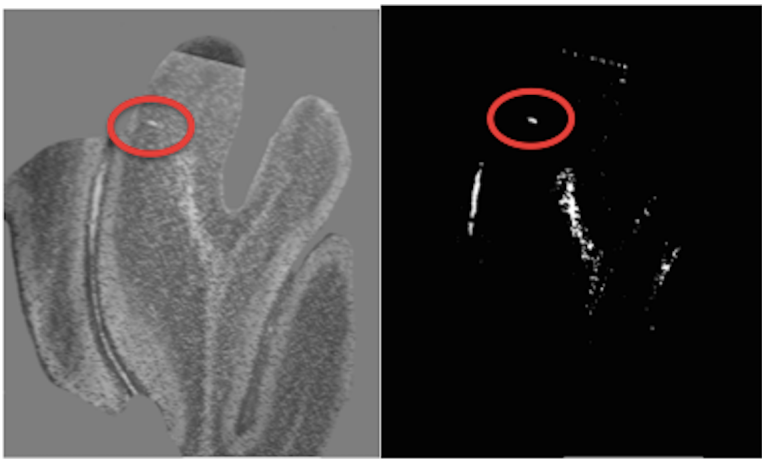

(a) Raw image (cerebellum) (b) Applied DoG

Figure 3.9: Example of DoG processing. This figure shows all high contrast blobs are segmented. Red circle indicates the vessel cross section. Note that all high-contrast objects (i.e. white binarized blobs) will be processed in the post-processing step in order to eliminate noise results.

these will be denoised at the post-processing step. To discriminate coherent structures from the mixture of the coherent structure and noise, we generated freehand masks of the cerebellum region, and then locally processed the cerebellum region with Difference of Gaussian (DoG) filter. DoG filtering is an effective edge sharpening method. Once the original images are blurred by convolving with DoG kernels that have different standard deviations, the blurred image are subtracted from the original images. As a result, DoG filtering extracts spatial information that contains the high-frequency domain (Figure 3.9.(b)).

3.3 Post-processing

This section describes partitioning of the volume, noise removal, and connecting the discontinuity (Figure 3.10). At first, we partition the volume into a manageable size. Second, we introduce a couple of novel ways to remove streaks and chatter. Third, we illustrate heuristics to connect discontinuities between the connected components (CCs). Finally, we apply artificial neural networks to remove the remaining noise. Figure 3.10 shows the post-processing workflow.

3.3.1 Partitioning the volume

This section discusses how we can handle large size of image volume data. In this thesis, we aim at processing the entire KESM Nissl data set. Also, we need to remove various sources of imaging artifacts (e.g. smear, streaks) in the 3D context. This is because we cannot simply determine each CC as a noise or vasculature in the 2D context (Figure 3.11). However, processing of the whole mouse brain in the 3D

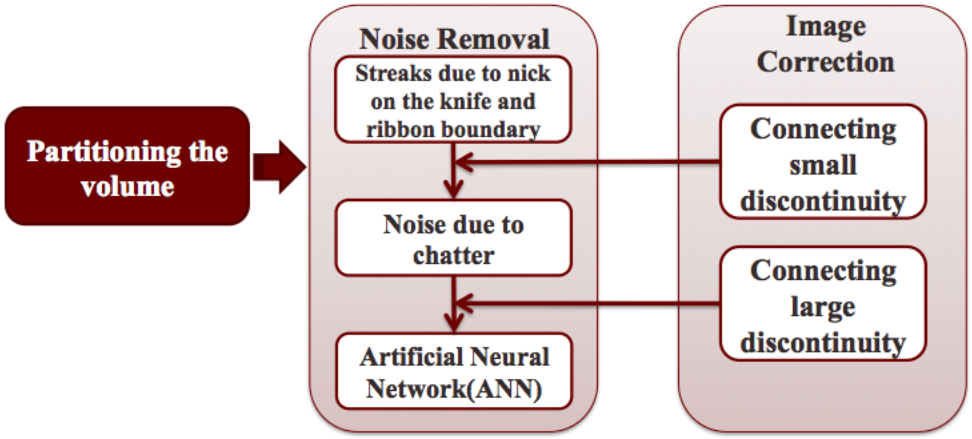

Figure 3.10: Workflow of post-processing

volume requires approximately 2TB of memory space. Therefore, special handling method is needed to extract the full vasculature networks in the 3D volume.

Many previous works have been done to reconstruct the KESM mouse brain data sets [4, 5, 3, 6]. But these works only processed the vascular networks in a small volume (e.g. $\sim$ 500 voxels $\times$ 500 voxels $\times$ 500 voxels).

In order to process the whole-brain scale volume, we decompose the volume into several subvolumes. Each sub volume is processed sequentially, and then these sub volumes are merged into the whole-brain scale volume later on.

3.3.2 Noise removal

After the thresholding step, all subsequent images are stacked to render a 3D volume. Since the proposed method is designed to segment all possible vessel cross sections, we need to eliminate noisy results among all detected foreground. Thus,

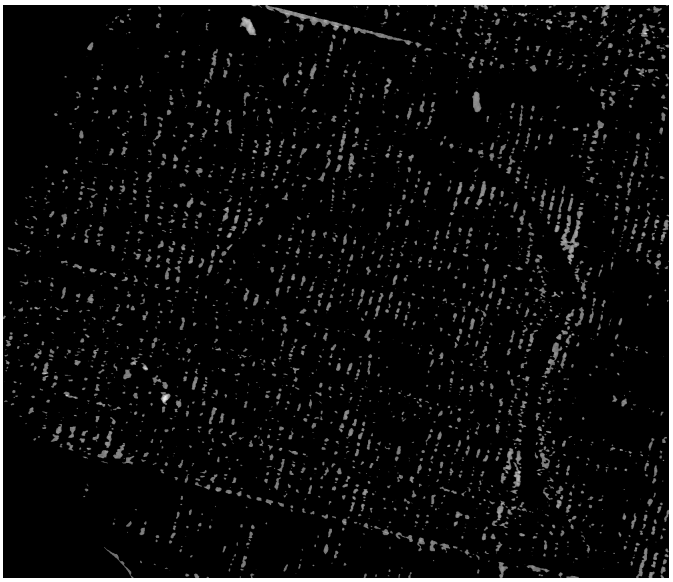

Figure 3.11: After initial thresholding. Discriminating each CC as a noise or vasculature is hard in the 2D context.

we try to detect vessel cross sections among the initially thresholded 3D volume. However, there is no clear difference between vessel cross sections and noise objects in the image sequence. Thus, we need to identify the vessel cross sections in the 3D context instead of in the 2D context.

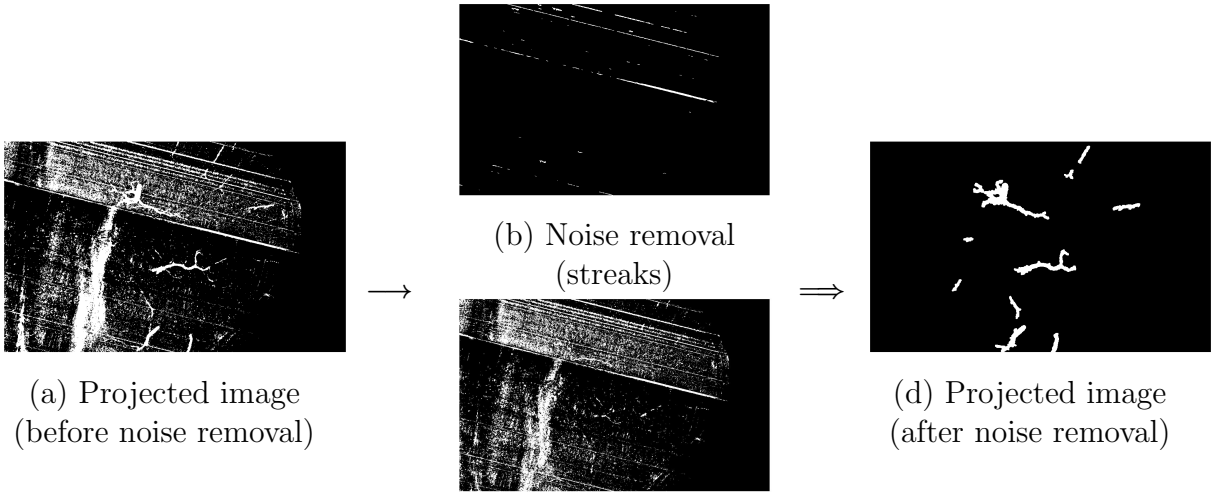

Figure 3.12: (a) shows the projected image of the 3D volume to the X-Y (2D) plane before noise removal. (b) shows the extracted component of the streaks that are projected into the X-Y plane. (c) shows the are extracted components of the 3D volume that are less than the threshold value. (d) shows the final results.

3.3.2.1 Streaks due to nick on the knife and ribbon boundary

The KESM mouse brain Nissl data set exhibits dark streaks due to nick on the diamond knife and ribbon boundary [1]. We developed a novel way to eliminate high-contrast streaks in the 3D volume.

The workflow of the noise reduction method for streaks is as follows: (1) projecting the 3D volume to X-Y (2D) plane, (2) and applying global thresholding algorithms. Note that the proposed method employs Otsu's method for thresholding, mean-based thresholding, and extended H-maxima thresholding. Otsu's method [30] is an automatic clustering-based image thresholding algorithm. Extended H-maxima is a geodesic transform that suppresses all maxima whose pixel value is smaller than

a given pixel value h [41]. (3) Extracting the binarized CC by calculating the regional properties of the CC. Regional properties are the set of type of measurement for each CC (e.g. the number of pixel in the region, the ratio of pixels in the region, and the angle between the x-axis and the major axis of the object). Since specific geometric properties of the streak (i.e. orientation, solidity, area, and eccentricity) have distinctive values different from those of the object of interest, we can extract the streaks by calculating the geometric properties of the projected component. In this case, each feature of the projected components is measured by *regionpros*, a MATLAB [42] built-in function. Typically, the streaks are roughly oriented between -13° to -14° with the eccentricity that is greater than 0.95 (between 0 to 1). (4) Once all coordinates of the pixels in the projected image (e.g. X-Y plane) are retrieved, the proposed method sets all corresponding 2D pixels, extracted from (3), to zero in the original 3D volume.

As a result, the streaks are removed from the original 3D volume. Figure 3.12.(b) shows the extracted streaks from the coronal cross-section.

3.3.2.2 Noise due to chatter

In this section, we describe how to get rid of noise due to chatter. Most sectioning techniques have a common issue during the cutting process: vibration of the diamond knife and the specimen. This vibration gives rise to a phenomenon called chatter, which is difficult to suppress. Chatter tends to appear as a periodic pattern across the image.

Previously, a couple of methods were developed to remove the noise due to chatter from the KESM rat Nissl data. Mayerich [35] used a customized local smoothing

technique that used the mean of a small window of pixels surrounding the center pixel in the image. As a result, the local window removed chatter as the window moved across the image. However, local smoothing is not feasible to apply to the KESM mouse brain Nissl data since high frequency details would be removed after applying this customized local smoothing window.

Lim [6] developed a simple heuristic, called guidance map. Before applying the guidance map, maximum-entropy algorithm [31] is employed to binarize the image. With the binarized image, Lim's method produces a new image, guidance map, by taking the minimum of the previous image and the subsequent image. Lim's method produces decent results if the image contrast is high enough. However, Lim's method only considers the previous and the subsequent image, not the whole 3D context. Therefore, his method cannot accurately distinguish the CC as noise or vascular segment. Furthermore, maximum-entropy algorithm provides poor segmentation performance if some vessel cross sections have low-contrast. This poor segmentation performance gives rise to frequent discontinuities along the vascular segment. This drawback is critical because the vessel cross section needs to be connected to those in the subsequent image. The vessel cross sections should continuously appear in the subsequent images with similar (x, y) coordinates, whereas noise is not likely to show up in the subsequent image.

In sum, both methods are not suitable for the KESM mouse brain Nissl data set because (1) high-frequency details could be removed significantly, and (2) noise is not adequately suppressed or eliminated. Therefore, we implement a simple, yet intuitive and effective method to remove the noise.

The proposed method goes through the following steps. (1) The proposed method measures centerline length along the axial direction of each connected component in the 3D volume. (2) If the CC is longer than the threshold, the CC will remain. Oth-

erwise, the CC will be eliminated. Note that the threshold value of axial length is empirically determined in advance. In this thesis project, we used 30 as a threshold value. Figure 3.12.(e) shows the extracted CC after noise removal.

However, some CCs, those that are shorter than the threshold, seem to be vascular segments in the 3D context. This is a common problem with thresholding-based segmentation when the image has low contrast. We should connect such disconnected vascular segments before applying this noise removal method. A detailed method of connecting the discontinuity will be specifically discussed in section 3.4

3.3.2.3 Artificial neural network

Finally, we apply a feed-forward artificial neural network (ANN) to discriminate objects of interest and remove residual noise that could not be eliminated by the previous steps. ANNs is a biologically inspired learning models and consists of many simple artificial neurons.

In this thesis project, we used the MATLAB neural networks toolbox [43]. The neural networks toolbox provides various tools: creating, training, visualizing, simulating, and analyzing the neural network. MATLAB NN toolbox also provides Multi-Layer Feed-forward (MLF) neural network. The MLF neural network trained using the back-propagation learning algorithm [44].

First, we fetch all CCs after the noise removal step. Note that the total number of CCs of the post processed 3D volume is around 6,000 and all CCs are measured in 3D volume since the noise components are not clearly distinguishable in the 2D context. For this reason, we measured three-dimensional geometric properties. Figure 3.13 shows the detailed information of the neural network. Intuitively, a human operator

could identify some CCs as a certain class (i.e. vasculature or noise) while the other CCs could not be classified as any class by a human operator. In case of which the CC is identifiable as a certain class, we manually label the CC to the corresponding class, and use it to train the neural network.

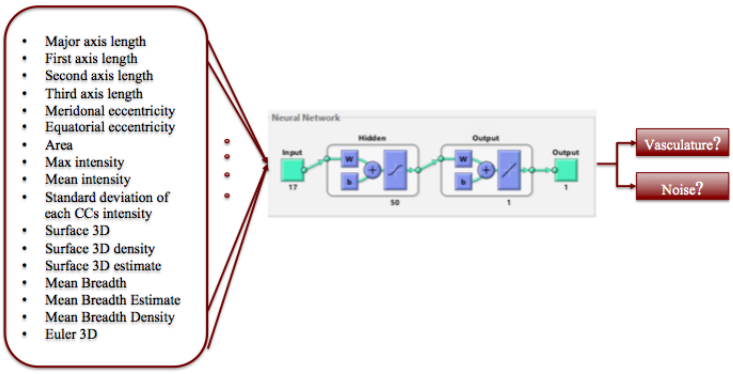

Figure 3.13: A block diagram of the ANN. We use 17 local geometric properties as input and 50 neurons as hidden layers. The outputs are scaled values that could be determined as vasculature or noise. The local geometric properties used as input were (1) major axis length, (2) first axis length, (3) second axis length, (4) third axis length, (5) meridional eccentricity (i.e. the eccentricity of the section through the longest and the shortest axes), (6) equatorial eccentricity (i.e. the eccentricity of the section through the second longest and the shortest axes), (7) area, (8) max intensity, (9) mean intensity, (10) standard deviation of each CC's intensity, (11) surface 3D, (12) surface 3D density, (13) surface 3D density estimate, (14) mean breadth (i.e. the mean breadth of the labeled CC), (15) mean breadth estimate (i.e. the estimate of mean breadth within the labeled CC), (16) mean breadth (i.e. the ratio of mean breadth over volume of the CC), and (17) euler 3D (i.e. the Euler number of the labeled CC). For the target output, the human labeled results as vasculature or noise were provided.

Next, we use local geometric properties to construct the input vectors to train the MLF neural network. To determine the number of optimal hidden neurons, we employ Cross-validation during training the network, which is necessary to test the

network with the same data but with different parameters. This process can help overcome the over-fitting problem.

We tested 0 to 100 neurons at step size of 10 to find out an optimal number of hidden neurons. We found that a reasonable number is 50. Although the trained network has slight over-fitting, the network performance reported in Figure 3.14 shows that the result is reasonable. As described in Figure 3.14, Mean-Squared Error (MSE) is very small, and the learning is fast. What is more, Figure 3.14 indicates that over-fitting starts to happen after iteration 3, where the best validation performance of the network occurs.

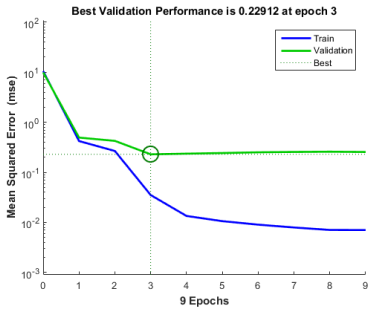

(a) Mean-Squared Error

Figure 3.14: Mean-Squared Error of the ANN

3.4 Connecting discontinuity

In this section, we describe a new method to address discontinuity between the connected components (CCs) in the 3D volume. As we mentioned in section 3.3.2.2, some disconnected segments are present because of low contrast. However, the disconnected components to should be connected to each other. There were two types

of discontinuities present in the volume: small discontinuity and large discontinuity. We defined small discontinuity as one or two missing vessel cross sections along the axial direction between two CCs. We defined large discontinuity as more than three missing vessel cross sections along the z-axis between two CCs, and upper bound of the discontinuity was empirically set to 30.

3.4.1 Connecting small discontinuity

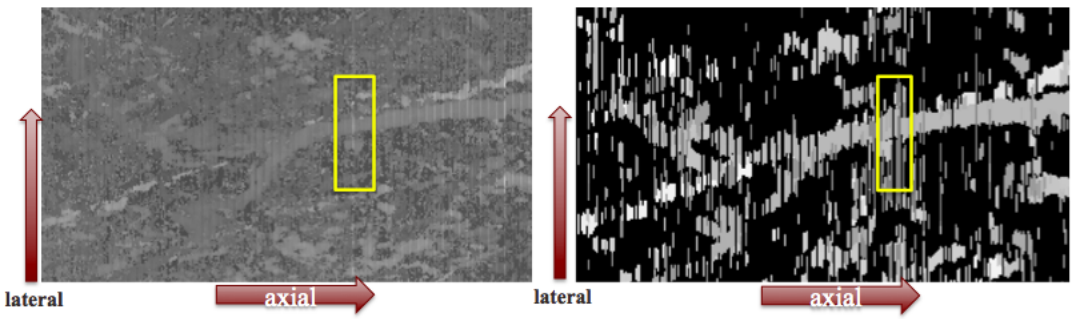

Figure 3.15: The left panel shows the sagittal view of the raw images. The right panel shows the sagittal view of the initial thresholding result. Yellow bounding boxes indicate the location of a small discontinuity

As shown in Figure 3.15, there are small discontinuities in the 3D volume along with the axial length. We applied simple heuristics to connect the small discontinuity. To connect the disconnected segments, the proposed method is designed to detect small discontinuities in each of the four consecutive images, and connect the disconnected segments under certain condition. Basic idea of the approach is as follows.

a. Let the four consecutive images be L_{n-1}, L_n, L_{n+1}, and L_{n+2}, where n is a positive integer (n=2,3,4,...) (Figure 3.16).

b. If L_{n-1} has a blob or more than one blob, the proposed method renders a bounding box, B_{n-1}, around the detected blob from L_{n-1}.

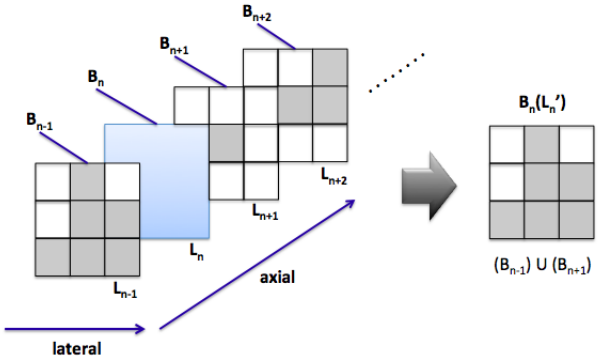

Figure 3.16: Example of connecting small discontinuity. Note that only B_n is empty among the four consecutive bounding boxes, but the others are filled with at least one pixel in the bounding box. B_n, will be replaced with a new image, the union of B_{n-1} and B_{n+1}. In this case, B_{n+2} will not be influenced by B_n.

c. Also, the proposed method renders the bounding boxes for L_n, L_{n+1}, and L_{n+2}, respectively, with the same size and coordinate of B_{n-1} from L_{n-1} (Figure 3.16).

d. If B_n or B_{n+1} is empty, the empty one will be replaced with the a bounding box that is generated by $(B_{n-1} \cup B_{n+1})$ or $(B_n \cup B_{n+2})$ (Figure 3.16).

e. If B_n and B_{n+1} are empty, B_n and B_{n+1} will be replaced with a new bounding box that is generated by $(B_{n-1} \cup B_{n+2})$ (Figure 3.17).

f. If B_{n+2} is empty, the proposed method will not fill in B_{n+2} because it is the last one among the four consecutive bounding boxes (Figure 3.18).

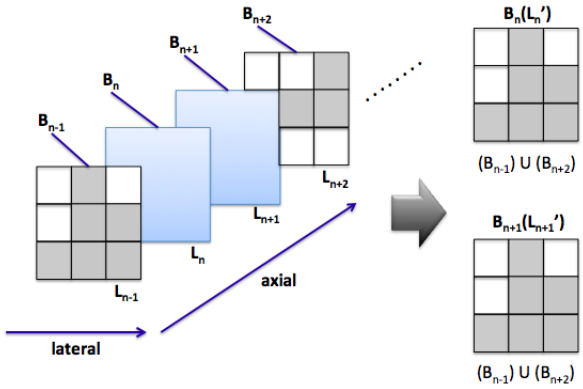

Figure 3.17: Example of connecting small discontinuity. Note that two bounding boxes, B_n and B_{n+1}, are empty. Thus, B_n and B_{n+1} will be replaced with a new image, the union of B_{n-1} and B_{n+2}.

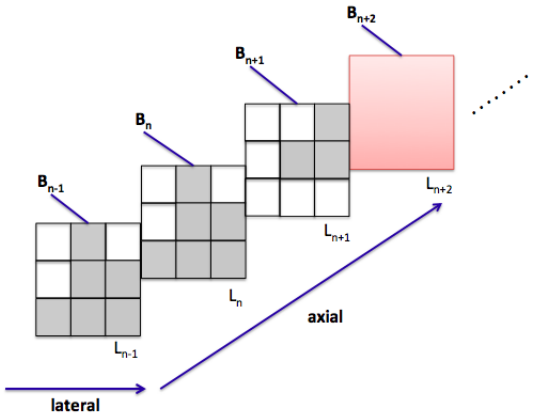

Figure 3.18: Example of connecting small discontinuity. Note that B_{n+2} from L_{n+2} is empty. In this case, L_{n+2} will not be filled with any pixel since subsequent bounding box of L_{n+2} does not exist.

In other words, if the discontinuity of the axial length is less than 3, the proposed method will attempt to connect the disconnected discontinuity. As a result, the small disconnected segments will be connected through the steps (a) to (e). The proposed method iteratively computes the bounding boxes, B_{n-1}, B_n, B_{n+1}, and B_{n+2}, based on the location (i.e. 2D coordinates) and size of B_{n-1}. Then, the proposed method conducts the same process from (a) to (e) until all bounding boxes from L_{n-1} are generated.

3.4.2 Connecting large discontinuity

In this section, we introduce a novel method to connect large discontinuity between the CCs in the 3D volume. As shown in the left panel of Figure 3.20, there are large gaps in the 3D volume along the Z-axis. To connect the disconnected segments, the proposed method measures the minimum Euclidean distance between the CCs in the 3D volume.

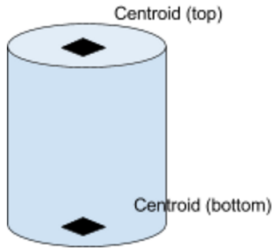

Figure 3.19: Top and bottom centroids in the connected component

Initially, the proposed method extracted two centroids from the top and the bottom of the bounding box of the n-th CC (Figure 3.19), where n is a positive

integer (n= 1,2,3,...), and sequentially stores the centroid information to the list. The basic idea of the distance measuring between the CCs is as follows (Figure 3.20).

The Euclidean distance between two points $C1 = (x, y, z)$ and $C2 = (a, b, c)$ in space is defined as $d(C1, C2) = \sqrt{(x-a)^2 + (y-b)^2 + (z-c)^2}$. The distance between a center point $C1$ and the other center point $C2$ is the Euclidean distance $d(C1, C2)$.

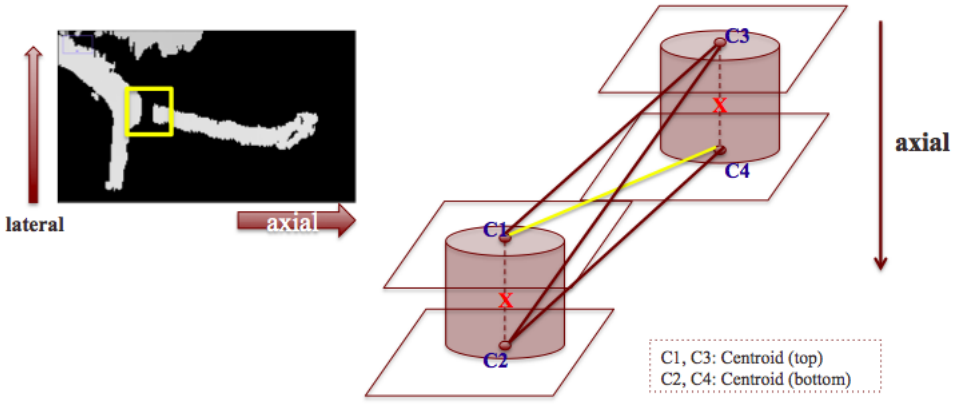

Figure 3.20: The left panel shows an example of large discontinuity. The right panel shows how to find the minimum Euclidean distance between the CCs.

a. Let the top of the centroid on the left side be the C1, and the bottom of the centroid on the left side be the C2.

b. Let the top of the centroid on the right side be the C3, and the bottom of the centroid on the left side be the C4.

c. In this case, the minimum Euclidean distance between the CCs is d(C1,C4). Note that if the centroids are not in the same CC, the proposed method will calculate

the Euclidean distance between the centroids. Otherwise, the distance between the centroids in the same CC will be disregarded.

d. Each minimum Euclidean distance between the CCs and the index of the CCs are stored in a list. Note that duplicated distances, such as d(C1,C3) and d(C3,C1) were removed.

e. Finally, the proposed method examines the minimum Euclidean distance of the discontinuity that is stored in the list. If the distance of the discontinuity is within the threshold value, then the proposed method will connect the discontinuity (Figure 3.21).

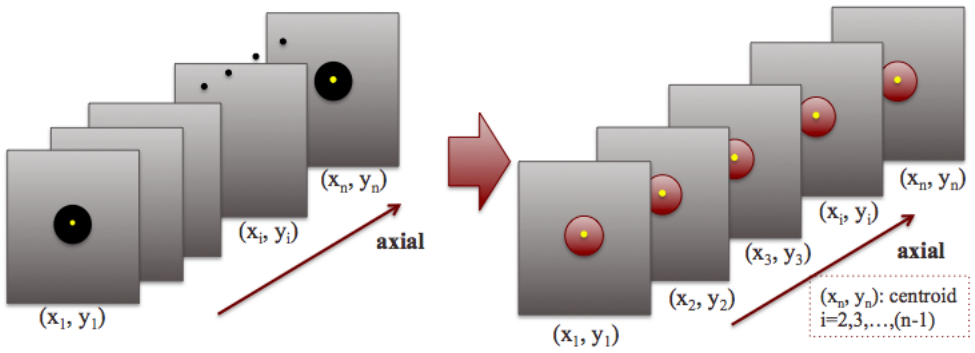

Figure 3.21: If there is a discrepancy between the initial centroid that are extracted from the 2D images and the predicted centroids (e.g. (x_2,y_2), (x_3, y_3), ..., (x_{n-1}, y_{n-1})), the bounding box of the predicted blob will be shifted. The location of the bounding box will be automatically adjusted once it reaches the end of the CC.

As shown in Figure 3.22, the large discontinuity will be connected through the steps (a) to (e).

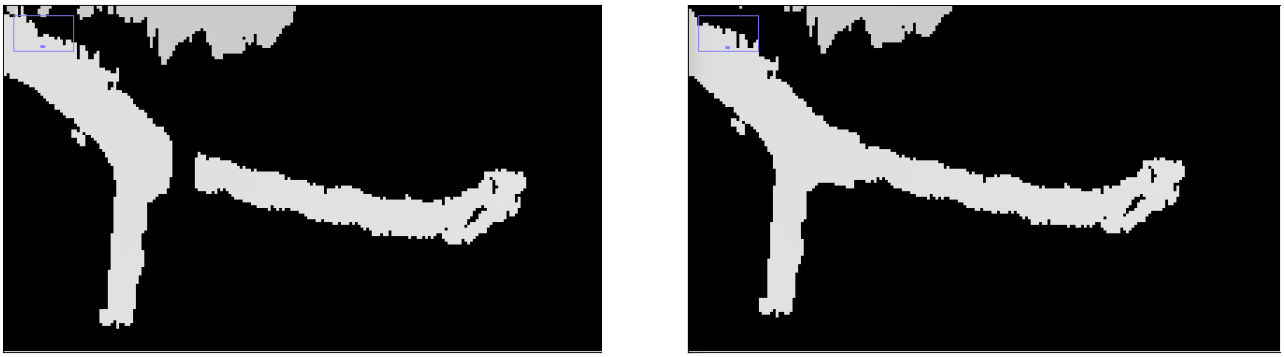

(a) Disconnected (Sagittal view)

(b) Connected (Sagittal view)

Figure 3.22: The left panel shows a sagittal view of the 3D volume with two disconnected components. The right panel shows a sagittal view of the 3D volume where two components are successfully connected by the proposed method.

4. RESULTS AND ANALYSIS

In this chapter, we analyze the reconstruction results of the KESM mouse Nissl data set. Also, we consider reconstruction results on the KESM rat Nissl data set compared to existing work (Lim's method [6]).

4.1 Reconstruction results of KESM mouse Nissl data set

Throughout the pre-processing, thresholding, and post-processing steps, we reconstructed microvasculatures in the KESM mouse Nissl data set at the whole-brain scale. Figure 4.1 shows the volume visualization of initial thresholding and post-processing. As shown in Figure 4.1(a)(c)(e), the volume visualization of initial thresholding does not have enough vasculatures even though the proposed method properly enhanced the image contrast, and intentionally lowered the threshold value to extract all possible vessel features. Nevertheless, some low-contrast vessel cross sections were still not distinguishable due to excessively low-contrast or being severely corrupted by imaging errors that cannot be corrected. However, overall, the proposed method gave reasonable results. To validate the proposed method, we need to analyze accuracy and integrity of the performance.

4.2 Analysis

In this section, we validate the performance of the proposed method by calculating precision, recall, and F-score of the reconstructed volume of the KESM mouse

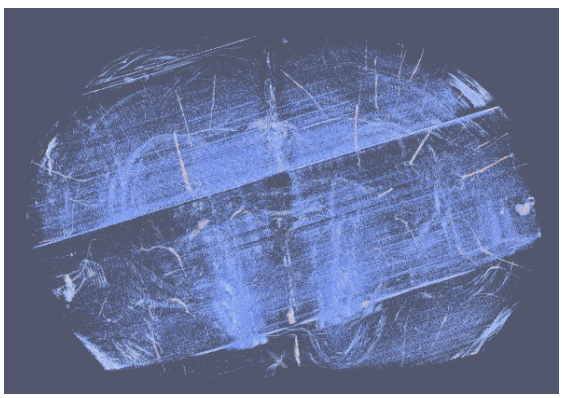

(a) Initial thresholding (posterior view)

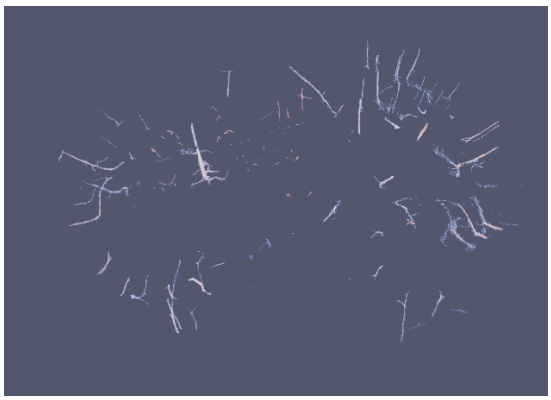

(b) Processed volume (posterior view)

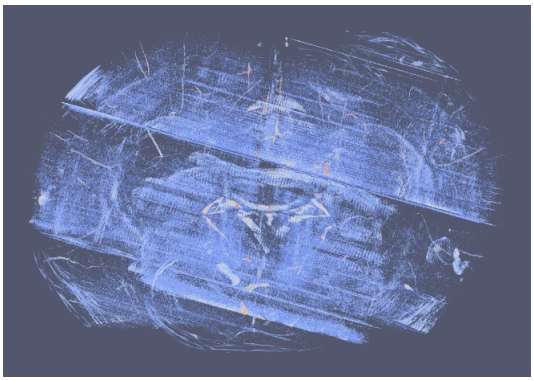

(c) Initial thresholding (anterior view)

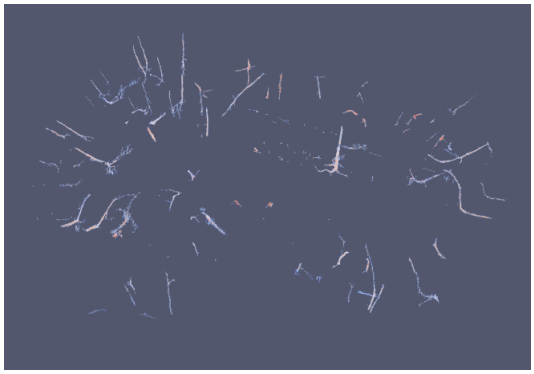

(d) Processed volume (anterior view)

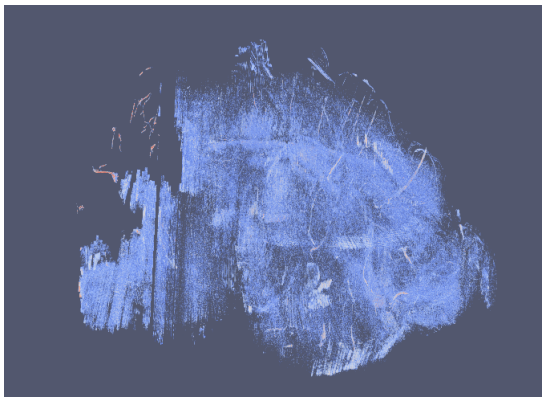

(e) Initial thresholding (sagittal view)

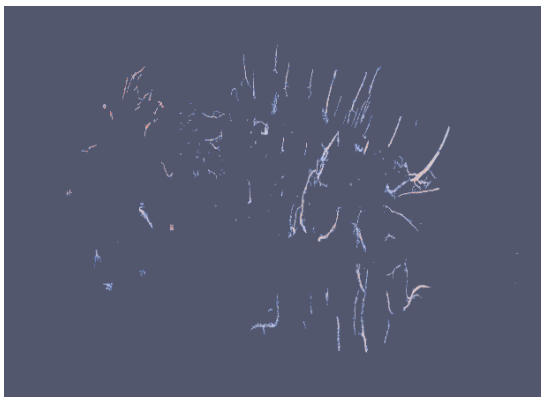

(f) Processed volume (sagittal view)

Figure 4.1: Volume visualization of the KESM mouse Nissl data. The left panels show different viewing angles of the initial thresholding results. The right panels show different viewing angles of the processed volume after noise removal.

Nissl data set.

Moreover, we compare performance of the proposed method with Lim's method using the KESM rat Nissl data set. We expect this comparison result to more precisely verify the performance of the proposed method because the KESM rat Nissl data set has higher contrast than the KESM mouse Nissl data set, although it is only a partial volume (somatosensory cortex). Finally, we examine noise robustness between Lim's method and the proposed method by analyzing statistics of the reconstructed results.

4.2.1 Validation of the KESM mouse Nissl data set

In this section, we introduce the validation method to quantify the performance of the proposed method. Statistical validation is important because it allows us to determine whether the method is effective for the reconstruction of microvascular network. In this thesis, we used precision, recall, and F-score to validate a performance of the proposed method in terms of microvasculartur extraction. Precision, recall, and F-Score are the basic measurements used in evaluating a binary classification accuracy of a classification method [49], detailed below [45].

$$Precision = \frac{TP}{TP+FP}$$

$$Recall = \frac{TP}{TP+FN}$$

$$F_\beta = (1+\beta^2) \cdot \frac{Precision \cdot Recall}{\beta^2 \cdot Precision + Recall}$$

where, true positive (TP) is the number of all correctly segmented cross sections, false positive (FP) is the number of all falsely identified cross sections, true negative

(TN) is the number of all non-vessel-cross-sections correctly labeled as such, false negative (FN) is the number of vessel cross sections falsely labeled as noise, and β is non-negative real value that is assigned as 2.

In detail, precision indicates the portion of true positive (TP) among all objects labeled as vessels cross sections, and recall indicates how many of the true vessel cross sections in the ground truth are detected [46]. F-score is a harmonic mean of precision and recall.

At first, we manually generated 900 ground truths. After that, every two-dimensional image and the corresponding human segmentation of ground truth were superimposed on each other. If there is an intersection of the blob in the superimposed image, the blob is labeled and counted. In an experiment on a volume (1000 pixels $\times$ 1000 pixels $\times$ 200 pixels) from the raw image sequence, the precision, precision recall, and F-score of the segmentation performance were 91.10%, 90.91%, and 90.99%, respectively. These scores indicate that the proposed method is promising.

4.3 Performance comparison of the proposed method against Lim's method

In this section, we compare the 3D reconstruction results of the proposed method against Lim's method from the same KESM rat Nissl data set. In the first part, we compare the results on a small volume (200 voxels $\times$ 200 voxels $\times$ 200 voxels) and then compare the results on a large volume (2200 voxels $\times$ 2600 voxels $\times$ 960 voxels). Following subsections will present details of the comparison for each scale. Note that we did not apply freehand masks and ANN to reconstruct the KESM rat Nissl data. This is because the KESM rat Nissl data that we used in this experiment is relatively noise free.

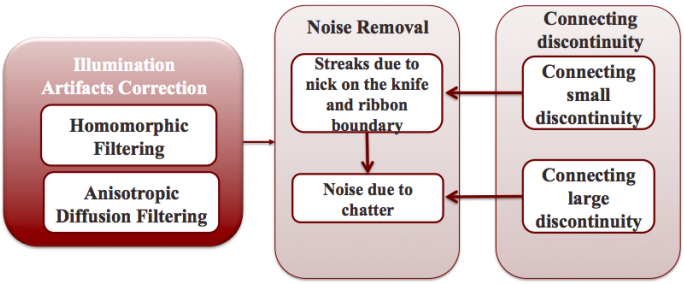

Figure 4.2: This block diagram shows the reconstruction workflow for the KESM rat Nissl data set. We selectively applied methods from the proposed method for the KESM mouse data. Note that ROI extraction and ANN were not utilized here.

4.3.1 Small data set

Firstly, we generated 200 ground truth images with local window (200 pixels $\times$ 200 pixels) by a human operator. Secondly, the reconstructed volume of the ground truth and the reconstructed volume generated by Lim's method were compared. Lastly, we estimated each reconstructed result by calculating precision, recall, and F-score (Figure 4.5). In the experiment on the reconstructed volume from Lim's method, precision, recall, and F-score of the segmentation performance were 69.64%, 83.29%, and 75.85%, respectively. In the experiment on the reconstructed volume from the proposed method, precision, recall, and F-score of the segmentation performance were 77.52%, 99.38%, and 87.09%, respectively.

Interestingly, the volume that was reconstructed by Lim's method (Figure 4.3) has frequent discontinuities. On the other hand, in the volume that was reconstructed by the proposed method, a large number of the discontinuities have been eliminated.

In sum, as exemplified in Figure 4.3 and 4.4, the results show that the proposed method outperforms Lim's method.

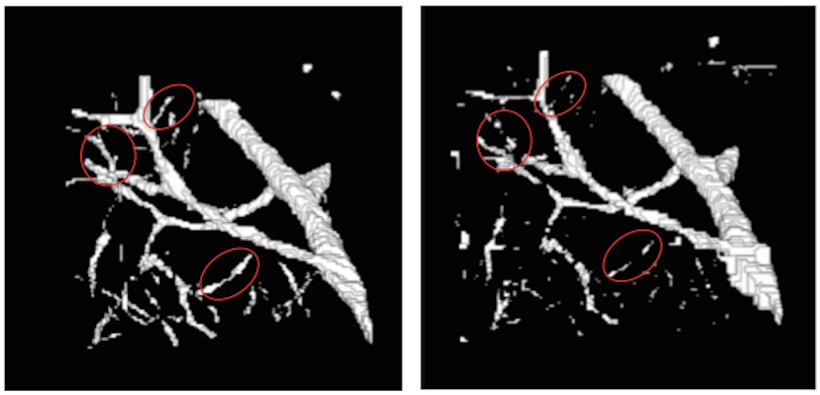

(a) Ground truth (b) Lim's method

Figure 4.3: (a) shows the stack of the ground truth images (200 voxels × 200 voxels × 200 voxels). (b) shows the stack of the generated images by Lim's method. The right panel has frequent discontinuities but in the left panel they are connected (red circles).

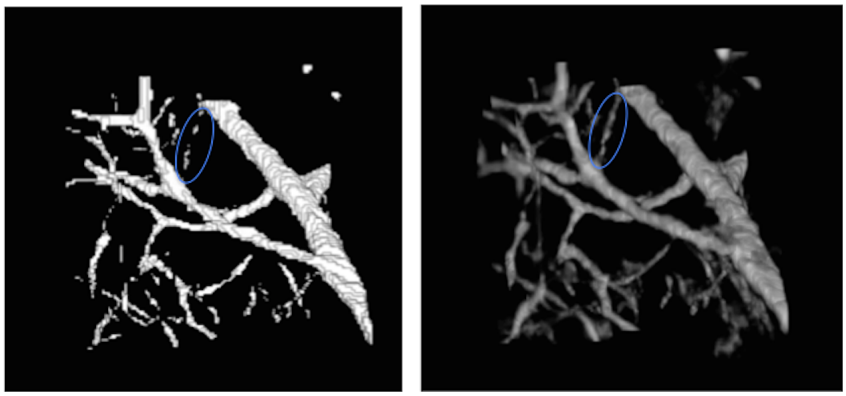

(a) Ground truth (b) Proposed method

Figure 4.4: (a) shows the stack of the ground truth images (200 voxels × 200 voxels × 200 voxels). (b) shows the stack of the generated images by the proposed method. Although we generated ground truth by a human operator, contrasts of some regions were quite ambiguous that led to several discontinuities. However, the proposed method overcame such issues (blue circles).

	Lim's method	Proposed method
Precision (%)	69.64	77.52
Recall (%)	83.29	99.38
F-score (%)	75.85	87.09

Figure 4.5: Comparison of Lim's method and the proposed method

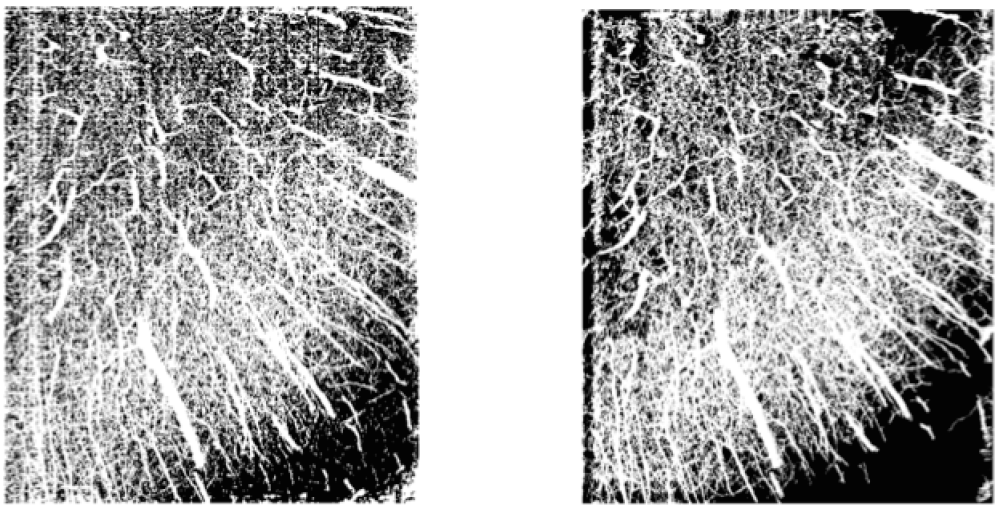

(a) Lim's method (b) Proposed method

Figure 4.6: Comparison results of the volume projection (binarized) into X-Y plane (2D). The left image shows the volume that is reconstructed by Lim's method. The right image shows the volume that is reconstructed by the proposed method.

4.3.2 Large data set

We further examined the results with large-scale data to verify the performance of the proposed result. As shown in Figure 4.6, it seems that the proposed method is more robust to imaging error than Lim's method, but the results still needed to be quantified. Therefore, we conducted a quantitative comparison in a large-scale volume (2200 voxels $\times$ 2600 voxels $\times$ 960 voxels). However, different quantitative analysis method should be utilized to compare the results because it is difficult to manually generate ground truth by a human operator in case of the large data set. In this thesis, we assumed a small size of the CCs is due to imaging error and the extracted CC has integrity if the centerline of the CC is long. With this assumption, we measured the centerline length and the number of voxel of each extracted CC to observe the error rate in the volume.

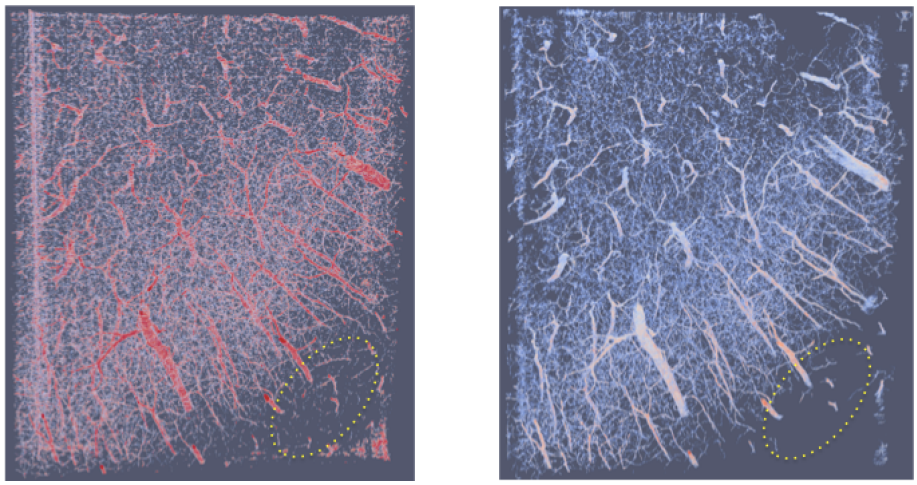

(a) Lim's method (b) Porposed method

Figure 4.7: Anterior view of the results of Lim's method compared to those of the proposed method. ParaView 4.1.0 64-bit [7], a 3D visualization framework, was used to visualize the data. Inside of the yellow circle, the left panel shows lots of noise, whereas the right panel shows that the noise has been removed.

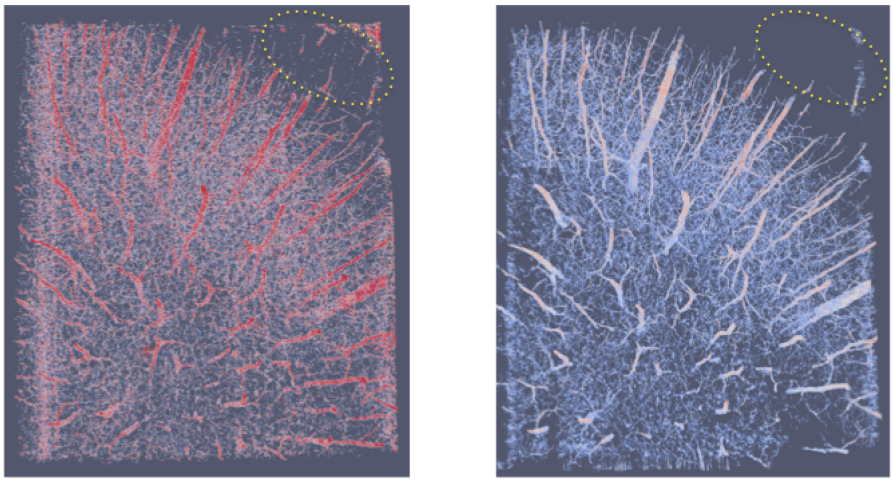

(a) Lim's method (b) Proposed method

Figure 4.8: Posterior view of the results from Lim's method and the proposed method. Inside the yellow circle, the left panel shows lots of noise, whereas the right panel shows that the noise has been removed.

As shown in Figure 4.7 and Figure 4.8, we can see in different viewing angles that the volume reconstructed by Lim's method has a large number of small discontinuities in the CCs, whereas the processed volume from the proposed method has not many small discontinuities. Also, in the close up view (Figure 4.9), we found that some vasculatures were disconnected from each other in Lim's method, while the topology of the vasculature in the proposed method was more likely to be preserved.

In order to quantify the difference between two distributions, we measured a centerline length and the number of pixel in the CC, and plot the results as a histogram. Let L be the centerline length and A be the total number of voxels in the CC. As shown in Figure 4.10.(a), Lim's method produces a large number of CCs with centerline length equal to 1 pixel (i.e. $L \leq 1$). On the other hand, the proposed method produces only few such CCs. As shown in Figure 4.10.(c), Lim's method produces a large number of small discontinuities (i.e. $A < 10$), while the proposed

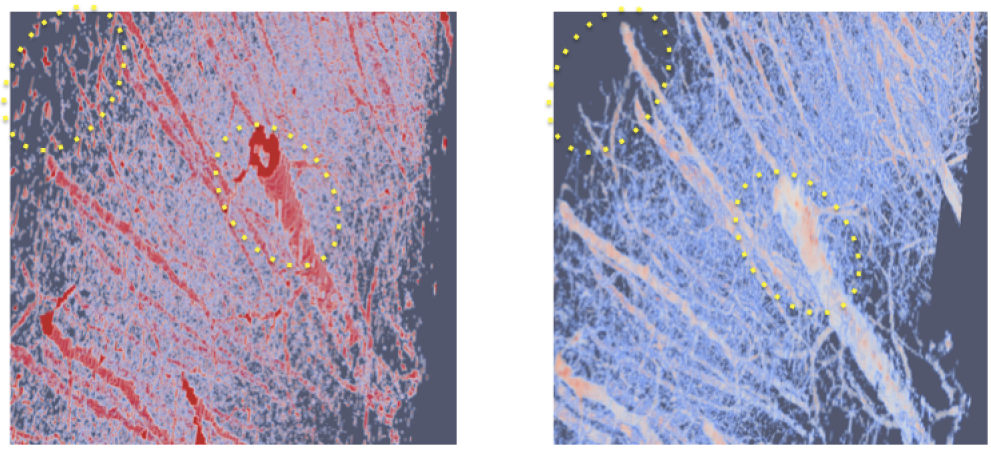

(a) Lim's method (b) Proposed method

Figure 4.9: Close up comparison between Lim's method and the proposed method

method produces fewer small discontinuities compared to Lim's method. Moreover, the proportion of CCs with long centerline (L>1000) in the volume that was generated by the proposed method is higher than that in Lim's method (Figure 4.10.(b)). This is because the proposed method connects the small and the large discontinuities while extracting the vasculature.

Moreover, Lim's method took 13 hours 22 minutes 5 seconds to process the KESM rat data set, while the proposed method took only 1 hour 20 minutes 27 seconds, which is nine times faster than Lim's method. The hardware used for the experiments had an Intel Core i7-4790K Quad-Core (4.0 GHz) processor, HDD 1TB 64MB Cache SATA 6.0Gb/s, and 16 gigabyte DDR3 RAM. All experiments were tested under Windows 10 Enterprise (64-bit) and Matlab 2016a.

To sum up, the proposed method is faster and more robust to noise than Lim's method.

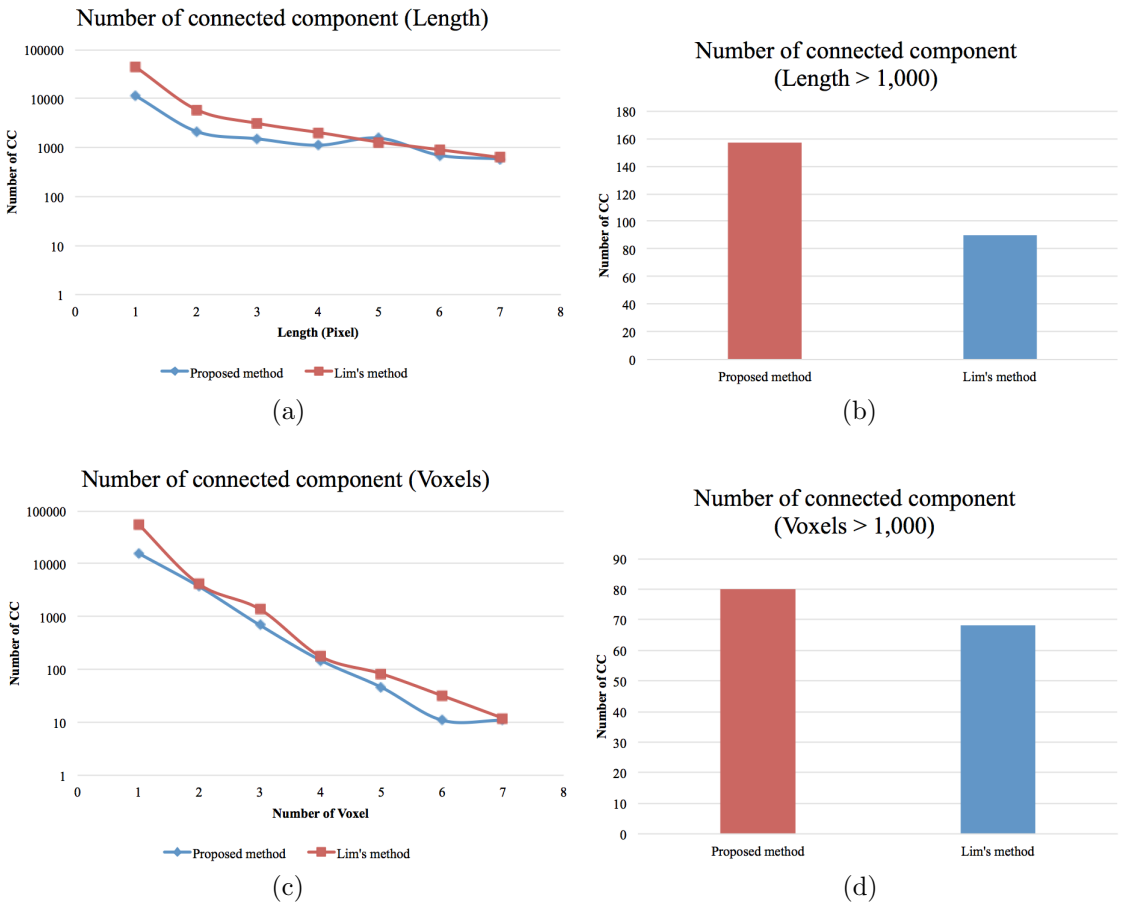

Figure 4.10: Figure (a) and (c) are log scale histograms that indicate the number of CCs in each volume as a function of CC length. The X-axis represents the centerline length of CC, and the Y-axis represents the number of CC in the volume (log scale). Figure (b) and (d) are frequency histograms that indicate the number of CCs with L>1000 for the two methods.

5. DISCUSSION

This thesis presents a novel vascular network reconstruction method for the KESM mouse and rat Nissl data sets. In this chapter, we discuss the contributions and open issues of the proposed method.

5.1 Contributions

In this thesis, we proposed a novel method to extract the vessel cross sections accurately and reconstruct 3D geometry of the vascular networks. This method provides an automated process to reconstruct the large-scale vascular network in the brain. Additionally, the proposed method enhances the image quality through a couple of noise removal and correction heuristics, which make the proposed method robust to noise. Moreover, this method is optimized for matrix operation, which reduces computation time.

5.2 Open issues and future works

5.2.1 Open issues

In this section, we discuss some open issues regarding the proposed method. As stated before, the proposed method provides accurate, efficient, and robust results. Despite these results, several problems have persisted: processing time, missing vasculature, and the presence of noise.

(1) Although the processing is much faster than the previous method [6], recon-

structing the KESM mouse brain Nissl volume data sets takes excessive time to deal with the high-resolution image data, which is not enough to process larger mammalian brains (e.g. dog, cat, and human brain). To solve this problem, GPU-based computing might be a good solution since it allows processing big data sets.

(2) Some vasculatures are removed by the proposed method due to low-contrast regions in the image sequence. Even though the proposed method enhances the original image and compensates the imaging error by connecting the discontinuities, some CCs have excessively low-contrast or imaging errors that could not be restored. A couple of factors caused this problem; poor staining, and mechanical malfunction of the microscope. To overcome these problems, enhancement of imaging performance of the KESM, or development of a novel staining method will help to solve the missing vasculature issue.

(3) Some false positives (i.e. noisy results) are still present in the reconstructed 3D volume due to background noise. Although we adopted homomorphic filtering and anisotropic diffusion to remove the high-frequency noise and low-frequency illumination artifacts, these artifacts remained in the background, and were not easily eliminated by the proposed method. Eventually, these artifacts are revealed as false positives after the neurovascular reconstruction step. To reduce the false positives rate, discrete wavelet transform (DWT) [47] can be considered. DWT is a localized transform at a limited scale that considers the local properties of the image. Although defining coefficients of each separable filter is difficult, DWT can be able to reduce the remaining noise if the image would properly decompose into the background (i.e. background noise) and the foreground (i.e. objects of interest).

5.2.2 Future work

As we validated the performance of the proposed method using the KESM rat Nissl data set, we anticipate that the proposed method can be used to analyze other data sets. For example, the proposed method can be applied to reconstruct neurovascular networks of the KESM mouse India-ink data set. Also, it can be utilized to other whole-brain mammalian Nissl data sets (e.g. mouse brain Nissl data from the Mouse Brain Architecture Project at Cold Spring Harbor Laboratory [8]). Figure 5.1 shows the example of both data sets.

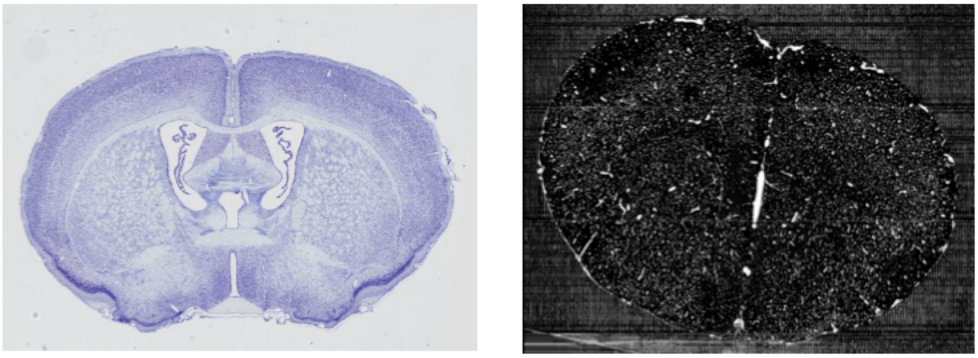

Figure 5.1: The left panel shows a coronal section from the Mouse Brain Architecture Project at Cold Spring Harbor Laboratory [8]. The right panel shows a coronal section from a KESM mouse India-ink data set.

In addition, the proposed method can be further developed to analyze both neuronal cell bodies and the vascular networks in the KESM mouse Nissl data set. In order to visualize the relationships between the cells and the vasculature, we can segment neuronal cell bodies, and then visualize the vascular network and the cell bodies in the same volume (Figure 5.2).

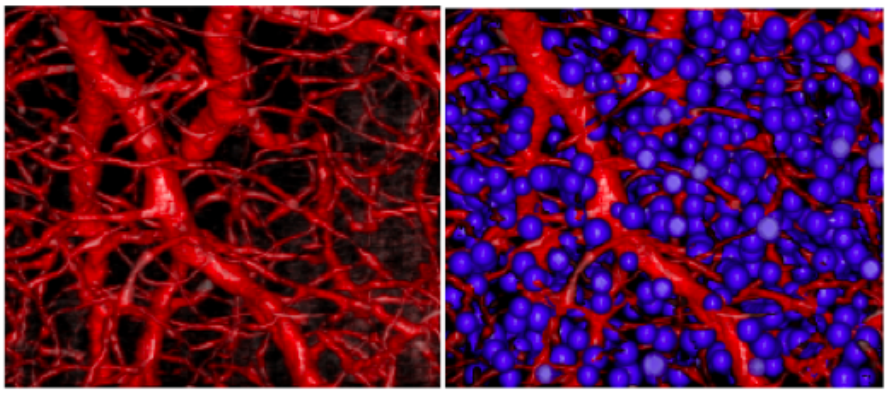

Figure 5.2: The left panel shows the volume visualization of a vascular network. The right panel shows the volume visualization of cell bodies and the vessels in the same volume. Adapted from [9].

6. CONCLUSION

In this thesis, we have successfully analyzed two data sets: the KESM whole mouse brain Nissl data set and the KESM partial rat brain Nissl data set. In sum, we pre-processed the KESM mouse Nissl data set by triaging corrupted image, extracting ROI, and correcting illumination artifacts. Next, we initially segmented the vessel cross section using dynamic global thresholding. After that, we applied a couple of heuristics to remove the streaks due to nick on the knife and ribbon boundary and the noise due to chatter, and corrected the image errors by connecting the discontinuous CCs in the microvascular networks. Lastly, artificial neural network was adopted to remove some remaining noise. To validate the proposed method, we compared the results with the volume processed by a previous method and the proposed method, using the KESM rat Nissl data set. The comparison results indicate that the proposed method is more robust to noise and nine times faster than the previous method. We expect that the proposed method will provide insights into analyzing microvascular networks in various types of mammalian brain.

REFERENCES

[1] D. M. Mayerich, *Imaging and computational methods for exploring sub-cellular anatomy*. PhD dissertation, Department of Computer Science and Engineering, Texas A&M University, College Station, Texas, 2009.

[2] Y. Choe, D. Mayerich, J. Kwon, D. E. Miller, J. R. Chung, C. Sung, J. Keyser, and L. C. Abbott, "Knife-edge scanning microscopy for connectomics research," in *Neural Networks (IJCNN), The 2011 International Joint Conference on*, pp. 2258–2265, IEEE, 2011.

[3] D. H. Han, *Rapid 3D tracing of the mouse brain neurovasculature with local maximum intensity projection and moving windows*. PhD dissertation, Department of Computer Science and Engineering, Texas A&M University, College Station, Texas, 2009.

[4] W. Yang, "Automated neurovascular tracing and analysis of the knife-edge scanning microscope india ink data set," MS thesis, Department of Computer Science and Engineering, Texas A&M University, College Station, Texas, 2014.

[5] A. Singhal, "Skeletonization-based automated tracing and reconstruction of neurovascular networks in knife-edge scanning microscope mouse brain india ink dataset," MS thesis, Department of Computer Science and Engineering, Texas A&M University, College Station, Texas, 2015.

[6] S. Lim, "Automated neurovascular tracing and analysis of the knife-edge scanning microscope rat nissl data set using ADA computing cluster," MS thesis, Department of Computer Science and Engineering, Texas A&M University, College Station, Texas, 2015.

[7] A. Henderson, J. Ahrens, and C. Law, *The ParaView Guide*. Kitware, Clifton Park, NY, 2004.

[8] P. Mitra, "The Mouse Brain Architecture Project," 2016. `http://mouse.brainarchitecture.org/`.

[9] D. M. Mayerich, L. Abbott, and J. Keyser, "Visualization of cellular and microvascular relationships," *Visualization and Computer Graphics, IEEE Transactions on*, vol. 14, no. 6, pp. 1611–1618, 2008.

[10] H. Wang, I. M. Hitron, C. Iadecola, and V. M. Pickel, "Synaptic and vascular associations of neurons containing cyclooxygenase-2 and nitric oxide synthase in rat somatosensory cortex," *Cerebral Cortex*, vol. 15, no. 8, pp. 1250–1260, 2005.

[11] J. A. Wells, H. E. Holmes, J. M. O'Callaghan, N. Colgan, O. Ismail, E. M. Fisher, B. Siow, T. K. Murray, A. J. Schwarz, and M. J. O'Neill, "Increased cerebral vascular reactivity in the tau expressing rtg4510 mouse: evidence against the role of tau pathology to impair vascular health in alzheimer's disease," *Journal of Cerebral Blood Flow & Metabolism*, vol. 35, no. 3, pp. 359–362, 2015.

[12] H. Girouard and C. Iadecola, "Neurovascular coupling in the normal brain and in hypertension, stroke, and alzheimer disease," *Journal of Applied Physiology*, vol. 100, no. 1, pp. 328–335, 2006.

[13] D. Mayerich, J. Kwon, Y. Choe, L. Abbott, and J. Keyser, "Constructing high resolution microvascular models," in *Third Workshop on Microscopic Image Analysis with Applications in Biology*, 2008.

[14] T. Hjornevik, T. B. Leergaard, D. Darine, O. Moldestad, A. M. Dale, F. Willoch, and J. G. Bjaalie, "Three-dimensional atlas system for mouse and rat brain imaging data," *Frontiers in Neuroinformatics*, vol. 1, p. 4, 2007.

[15] D. Mayerich, L. Abbott, and B. McCormick, "Knife-edge scanning microscopy for imaging and reconstruction of three-dimensional anatomical structures of the mouse brain," *Journal of Microscopy*, vol. 231, no. 1, pp. 134–143, 2008.

[16] G. Knott and C. Genoud, "Is EM dead?," *Journal of Cell Science*, vol. 126, no. 20, pp. 4545–4552, 2013.

[17] E. D. Boorman, M. F. Rushworth, and T. E. Behrens, "Ventromedial prefrontal and anterior cingulate cortex adopt choice and default reference frames during sequential multi-alternative choice," *Journal of Neuroscience*, vol. 33, no. 6, pp. 2242–2253, 2013.

[18] J. R. Chung, C. Sung, D. Mayerich, J. Kwon, D. E. Miller, T. Huffman, J. Keyser, L. C. Abbott, and Y. Choe, "Multiscale exploration of mouse brain microstructures using the knife-edge scanning microscope brain atlas," *Frontiers in Neuroinformatics*, vol. 5, pp. 84–100, 2011, Program No. 516.3.

[19] Y. Choe, L. C. Abbott, D. Han, P.-S. Huang, J. Keyser, J. Kwon, D. Mayerich, Z. Melek, and B. H. McCormick, "Knife-edge scanning microscopy: high-throughput imaging and analysis of massive volumes of biological microstructures," *In A. Ravi Rao and Guillermo Cecchi, editors, High-Throughput Image Reconstruction and Analysis: Intelligent Microscopy Applications*, pp. 11–37, 2008.

[20] Y. Choe, L. Abbott, D. Miller, D. Han, H. Yang, J. Chung, C. Sung, D. Mayerich, J. Kwon, and K. Micheva, "Multiscale imaging, analysis, and integration of mouse brain networks," in *Neuroscience Meeting Planner*, Society for Neuroscience San Diego, CA, Program No. 516.3, 2010.

[21] L. Abbott, "High-throughput imaging of whole small animal brains with the knife-edge scanning microscope," in *Neuroscience Meeting Planner*, Society for

Neuroscience Washington, DC, 2008, Program No. 504.2.

[22] Y. Choe, D. Han, P. Huang, J. Keyser, J. Kwon, D. Mayerich, and L. Abbott, "Complete submicrometer scans of mouse brain microstructure: neurons and vasculatures," in *Neuroscience Meeting Planner*, Society for Neuroscience Chicago, IL, 2009, Program No. 389.10.

[23] A. Kádár, G. Wittmann, Z. Liposits, and C. Fekete, "Improved method for combination of immunocytochemistry and nissl staining," *Journal of Neuroscience Methods*, vol. 184, no. 1, pp. 115–118, 2009.

[24] W. Zhang, "Real-time image error detection in knife-edge scanning microscope," MS thesis, Department of Computer Science and Engineering, Texas A&M University, College Station, Texas, 2014.

[25] A. Roebroeck, R. Galuske, E. Formisano, O. Chiry, H. Bratzke, I. Ronen, D.-s. Kim, and R. Goebel, "High-resolution diffusion tensor imaging and tractography of the human optic chiasm at 9.4 t," *Neuroimage*, vol. 39, no. 1, pp. 157–168, 2008.

[26] B. H. McCormick, "Development of the brain tissue scanner," *Technical Report, Laboratory, Department of Computer Science, Texas A&M University, College Station, Texas*, 2002.

[27] W. Zhang, J. Yoo, J. Keyser, L. C. Abbott, and Y. Choe, "Real-time detection of imaging errors in the knife-edge scanning microscope through change detection," in *Biomedical Imaging (ISBI), 2015 IEEE 12th International Symposium on*, pp. 177–181, IEEE, 2015.

[28] J. Shan, H.-D. Cheng, and Y. Wang, "A novel automatic seed point selection algorithm for breast ultrasound images," in *Pattern Recognition, 2008. ICPR*

2008. 19th International Conference on, pp. 1–4, IEEE, 2008.

[29] R. Xiao, J. Yang, M. Goyal, Y. Liu, and Y. Wang, "Automatic vasculature identification in coronary angiograms by adaptive geometrical tracking," *Computational and Mathematical Methods in Medicine*, vol. 2013, 2013.

[30] N. Otsu, "A threshold selection method from gray-level histograms," *Automatica*, vol. 11, no. 285-296, pp. 23–27, 1975.

[31] C. H. Li and C. Lee, "Minimum cross entropy thresholding," *Pattern Recognition*, vol. 26, no. 4, pp. 617–625, 1993.

[32] J. P. Lewis, "Fast template matching," in *Vision Interface 95*, vol. 95, (Canadian Image Processing and Pattern Recognition Society, Quebec City, Canada), pp. 120–123, 1995.

[33] D. Comaniciu and P. Meer, "Mean shift: A robust approach toward feature space analysis," *Pattern Analysis and Machine Intelligence, IEEE Transactions on*, vol. 24, no. 5, pp. 603–619, 2002.

[34] J. A. Sethian, *Level set methods and fast marching methods: evolving interfaces in computational geometry, fluid mechanics, computer vision, and materials science*, vol. 3. Cambridge university press, 1999.

[35] D. Mayerich, B. H. McCormick, and J. Keyser, "Noise and artifact removal in knife-edge scanning microscopy," in *Biomedical Imaging: From Nano to Macro, 2007. ISBI 2007. 4th IEEE International Symposium on*, pp. 556–559, IEEE, 2007.

[36] R. C. Gonzalez and R. E. Woods, *Digital image processing*. Pearson, New York City, New York, 2002.

[37] P. Perona and J. Malik, "Scale space and edge detection for visual scene analysis," in *Proc. IEEE Computer Society Workshop on Computer Vision*, pp. 16–22, 1987.

[38] P. K. Sahoo, S. Soltani, and A. K. Wong, "A survey of thresholding techniques," *Computer vision, graphics, and image processing*, vol. 41, no. 2, pp. 233–260, 1988.

[39] T. R. Singh, S. Roy, O. I. Singh, T. Sinam, and K. Singh, "A new local adaptive thresholding technique in binarization," *arXiv preprint arXiv:1201.5227*, 2012.

[40] S. Wu and A. Amin, "Automatic thresholding of gray-level using multistage approach," in *Document Analysis and Recognition, 2003. Proceedings. Seventh International Conference on*, pp. 493–497, IEEE, 2003.

[41] P. Soille, *Morphological image analysis: principles and applications*. Springer Science & Business Media, New York, 2013.

[42] M. Grant, S. Boyd, and Y. Ye, "Cvx: Matlab software for disciplined convex programming," 2008, Online.

[43] M. H. Beale, M. T. Hagan, and H. B. Demuth, "Neural network toolbox users guide," in *R2012a, The MathWorks, Inc., 3 Apple Hill Drive Natick, MA 01760-2098*, Citeseer, 2012.

[44] R. Hecht-Nielsen, "Theory of the backpropagation neural network," in *Neural Networks, 1989. IJCNN., International Joint Conference on*, pp. 593–605, IEEE, 1989.

[45] R. Jizba, "Measuring search effectiveness," *Creighton University Health Sciences Library and Learning Resources Center, Omaha, NE*, 2000.

[46] J. Yuan, S. S. Gleason, and A. M. Cheriyadat, "Systematic benchmarking of aerial image segmentation," *Geoscience and Remote Sensing Letters, IEEE*, vol. 10, no. 6, pp. 1527–1531, 2013.

[47] A. N. Akansu and R. A. Haddad, *Multiresolution signal decomposition: transforms, subbands, and wavelets*. Academic Press, San Diego, CA, 2001.